Atmospheric
Chemistry
and Physics
Discussions

A Global Evaluation of Daily to Seasonal Aerosol and Water Vapor Relationships Using a Combination of AERONET and NAAPS Reanalysis Data

Juli I. Rubin[1], Jeffrey S. Reid[2], Peng Xian[2], Christopher M. Selman[1], and Thomas F. Eck[3,4]

[1]U.S. Naval Research Laboratory, Washington, DC, 20375, USA
[2]U.S. Naval Research Laboratory, Monterey, CA, 93943, USA
[3]NASA Goddard Space Flight Center, Greenbelt, MD, 20771, USA
[4]Goddard Earth Sciences Technology and Research (GESTAR) II, University of Maryland Baltimore County, Baltimore, MD 21250, USA

Correspondence to: Juli I. Rubin (juli.rubin@nrl.navy.mil)

Abstract. The co-transport of aerosol particles and water vapor has long been noted in the literature, with a myriad of implications from air mass characterization to radiative transfer. In this study, the relationship between aerosol optical depth (AOD) and precipitable water vapor (PW) is evaluated to our knowledge for the first time globally, at daily to seasonal levels using approximately 20 years of AERONET observational data and the 16-year NAAPS reanalysis v1.0 (NAAPS-RA) model fields. The combination of AERONET observations with small associated uncertainties and the reanalysis fields with full global coverage is used to provide a best estimate of the seasonal AOD and PW relationships, including an evaluation of correlations, slope, and PW probability distributions for identification of statistically significant differences in PW for high AOD events. The relationships produced from the AERONET and NAAPS-RA datasets were compared against each other and showed consistency, indicating that the NAAPS-RA provides a realistic representation of the AOD and PW relationship. The initial analysis is then extended to layer AOD and PW relationships for proxies of the planetary boundary layer, and lower, middle and upper free troposphere. It was found that the dominant AOD and PW relationship is positive, supported by both AERONET and model evaluation, which varies in strength by season and location. These relationships were found to be statistically significant and present across the globe, observed on an event by event level. Evaluations at individual AERONET sites implicate synoptic-scale transport as a contributing factor in these relationships at daily levels. Negative AOD and PW relationships were identified and predominantly associated with regional dry season timescales in which biomass burning is the predominant aerosol type. This is not an indication of dry air association with smoke aerosol for an individual event, but is more a reflection of the overall dry conditions leading to more biomass burning and higher associated AOD values. Stronger correlations between AOD and PW are found when evaluating the data by vertical layers, including boundary layer, lower/middle/upper free troposphere (corresponding to typical water vapor channels), with the largest correlations observed in the free troposphere-indicative of aerosol and water vapor transport events. By evaluating variability between PW and relative humidity in the NAAPS-RA, hygroscopic growth was found to 1) amplify positive AOD-PW relationships, particularly in the mid-latitudes; 2) diminish negative relationships in dominant biomass burning regions; and 3) leads to statistically insignificant changes in PW for high AOD events in ocean regions. The importance of hygroscopic growth in these relationships indicates that PW is a useful tracer for AOD, but not necessarily as strongly for aerosol mass. Synoptic-scale African dust events are an exception where PW is a strong tracer for aerosol shown by strong relationships even with hygroscopic affects. Given this results, PW can be exploited in coupled aerosol and meteorology data assimilation for AOD and the collocation of aerosol and water vapor should be carefully taken into account when evaluating radiative impacts of aerosol, with the season and location in mind.

Atmospheric
Chemistry
and Physics
Discussions

1.0- Introduction

The definition of an aerosol is that it is a colloidal system of particles or droplets suspended in a dispersed gaseous medium (American Meteorological Society, 2020). While the word "aerosol" is often taken to represent only the particulate phase, the true definition reminds us of the thermodynamic, compositional and radiative "whole" that makes up the particulate and dispersed phases of an aerosol parcel. With this definition in mind, an important aspect of aerosol parcels that should be considered is the covariability between the aerosol particles and the dispersed water vapor. While the aerosol and water vapor relationship is generally accounted for in the context of relative humidity, hygroscopicity, and optical properties (e.g., Hänel et al., 1976; Charlson et al. 1992), the covariability of aerosol particles and dispersed water vapor is important in its own right. Early studies of co-located aerosol and water vapor measurements demonstrated the structural covariability between the two components (e.g, Stull and Eloranta 1984; Kleinman and Daum, 1991; Turner 2002; De Tomasi and Perrone, 2003). Now, coupled aerosol-water vapor profiles are commonly used to infer aerosol layer structure (e.g., Livingston et al., 2003; Reid et al., 2003; 2008; 2019; Wang et al. 2012; Yufeng et al., 2018), cloud detrainment (Su et al., 2011; Reid et al., 2019; He et al., 2021) and mixed layer properties (Späth et al., 2016). Even integrated aerosol optical depth (AOD) and precipitable water vapor (PW) comparisons have utility and have been used to identify air masses, transport pathways, and aerosol optical properties. Regional studies include Africa (Kumar et al., 2017, Xian et al. 2020), the Amazon (Kaufman and Frasier, 1997; Martins et al., 2018), India (Kumar et al., 2013; and Kannemadugu et al., 2015), and North America (O'Neil et al., 1993; Smirnov et al., 1994). Notable examples of co-transport of aerosol particles and water vapor include the African Monsoon Multidisciplinary Analysis (AMMA) in which elevated biomass burning aerosol layers were found with higher water vapor concentrations than the surrounding air (Kim et al. 2009). Likewise, Marsham et al., 2016 investigated water vapor enhancements with dust in the Saharan Air Layer (SAL).

It should be noted that higher PW amounts are typically associated with higher cloud cover fractions. These higher cloud fractions create additional environmental conditions for enhancements of the aerosol AOD and PW relationship. There is a high RH halo around cumulus clouds (Radke and Hobbs, 1991; Perry and Hobbs, 1996) which increases the near cloud hygroscopic growth of aerosol. Additionally, the passage of aerosol through clouds by convection and/or advection also increases hygroscopic growth. Cloud processing of particles in cloud droplets and new particle formation from gas-to-particle reactions in cloud water droplets are also important. Examples of remote sensing observations from AERONET of cloud processing increasing AOD in layer clouds and/or fog are given in Eck et al. (2012) and in the vicinity of cumulus clouds in Eck et al. (2014). Additionally high AOD events were often found to be associated with clouds in East Asia (Eck et al., 2019; Arola et al., 2017).

In addition to its utility as a tracer for transport and mixing, the aerosol particle-water vapor co-transport are significant in regards to their relative contributions to overall solar and terrestrial radiative effects (Rosario et al., 2011; Marsham et al., 2016; Deaconu et al., 2019; Gutleben et al., 2019; Granados-Muñoz et al., 2019; Zhu et al., 2019; Yu et al., 2021). Similarly, co-transport must be considered in atmospheric correction of land, ocean and atmospheric products

Atmospheric
Chemistry
and Physics
Discussions

80   (e.g., Sobrino et al. 1993; Eck and Holben 1994; DeSouza-Machado et al., 2006; Luo et al, 2019; Zeng et al., 2017;

81   Patadia et al., 2018; Frouin et al. 2019, Ibrahim et al. 2019; Miller et al. 2019). As previously noted, there are also

82   links to cloud development and potentially indirect effects (Ten Hoeve et al., 2011; Pistone et al., 2016). Ultimately,

83   the coupled aerosol particle- water vapor system must be considered jointly to adequately contain overall climate

84   budgets and forcing (Kaufman and Fraser, 1997; Wong et al., 2009; Schneider et al, 2010; Sherwood et al, 2010;

85   Haywood et al., 2011; Huttunen et al., 2014; Yu et al., 2014; Spyrou 2018).

86

87   Finally, recent advances in coupled data assimilation (DA) allow for not only a joint analysis of aerosol particles and

88   water vapor as is done in weakly coupled approaches, but for observations to jointly influence posteriors through

89   cross-covariances in strongly coupled DA (Liu et al., 2011; Lee et al., 2017; Ménard et al., 2019). The hope is that

90   strongly coupled DA can be used to generate a more consistent representation of coupled atmospheric systems. In the

91   context of the aforementioned references on the coupled aerosol particle-water vapor system, there is now a more

92   pressing need for evaluating joint aerosol and water vapor measurements. This is further emphasized by the observed

93   frequency of aerosol and water vapor co-transport in both forecast models and satellite observations. Similar spatial

94   patterns between aerosol optical depth (AOD) and precipitable water vapor (PW) can be observed on a daily basis in

95   model analyses, forecasts, and satellite products such as the Morphed Integrated Microwave Imagery at CIMSS - Total

96   Precipitable Water (MIMIC-TPW) (Wimmers et al. 2011), particularly associated with mid-latitude fronts. An

97   example of forecasts of TPW and AOD from the Navy Global Environmental Model (NAVGEM) (Hogan et al. 2014)

98   and Navy Aerosol Analysis Prediction System (NAAPS; Lynch et al. 2016), respectively are shown in Figure 1 in

99   which co-transport regions are highlighted. Aerosol and water vapor relationships are not expected to be universal and

100   will likely vary in magnitude from air mass to air mass due to differences in sources, physics, and overall vertical

101   distribution. While the previously mentioned studies have found relationships between aerosol and water vapor for a

102   host of case or local studies, this relationship has not to our knowledge been evaluated on a larger spatial and temporal

103   scale for broad applicability for aerosol forecasting and data assimilation.

104

105   This is the first of several studies developing coupled data analysis and assimilation of the water vapor- aerosol particle

106   system. Here, the project begins by focusing on observations of synoptic scale temporal and spatial relationships using

107   the extensive NASA Aerosol Robotic Network (AERONET; Holben et al., 1998; Giles et al., 2019). The advantage

108   of AERONET for this study is that the data record is long and includes high frequency ground-based measurements

109   of both aerosol in the form of AOD and water vapor in the form of PW with sites located across the globe. Additionally,

110   AERONET measurements are made throughout the entire daylight hours when the sun is not obscured by clouds. It

111   should be noted that this does result in a high pressure bias in AERONET data since few measurements are possible

112   in extensive cloud fraction conditions. Another important advantage is that the observations can be made effectively

113   in the near vicinity of clouds without the commonly observed satellite measurement artifacts of multiple scattering

114   between clouds, molecules, and particles which enables a minimization of cloud contamination in the near vicinity of

115   clouds as compared to satellite observations. While the AERONET network is extensive, it cannot provide a full global

116   evaluation of the aerosol and water vapor relationship. Therefore, the relationships identified in the AERONET dataset

117   are compared against model AOD and PW relationships found in the NAAPS reanalysis (NAAPS-RA) dataset (Lynch

Atmospheric
Chemistry
and Physics
Discussions

118   et al. 2016). A description of both the AERONET and NAAPS-RA datasets and the analyses conducting for

119   quantifying the global AOD and PW relationships are described in the Methods section below. The results of the

120   analysis are discussed in the context of large-scale relationships between column-integrated AOD and PW. A follow-

121   on study will then take the relationships found in this work and move on to evaluate the relationships on an event level

122   in space and time as well as the controlling factors that drive the aerosol and water vapor relationship, in particular,

123   how much synoptic scale transport controls the observed covariability.

124

125   **2 Methods**

126   In order to evaluate the relationship between column-integrated aerosol and water vapor in space and time, the

127   AERONET observational network is used as it provides joint measurements of aerosol and water vapor with low

128   levels of uncertainty, has a large number of sites located across the globe, and a long data record. While AERONET

129   measurements are column-integrated, they provide a good starting point for understanding the observed aerosol and

130   water vapor relationships at locations across the globe. As a first step, relationships are quantified at AERONET sites

131   between daily-averaged AOD and PW measurements. The focus here is on the synoptic-scale relationships between

132   aerosol and water vapor. Therefore, daily-averaged relationships are evaluated in this analysis, using correlations and

133   an evaluation of the water vapor probability distributions to identify statistically significant changes in PW with AOD.

134   The evaluation is then extended to the NAAPS-RA dataset in order to provide a more complete global perspective in

135   the full column as well as in different vertical components of the atmosphere, including the boundary layer and free

136   troposphere, as a means to understand how these relationships vary when considering vertical position. Finally, the

137   impact of relative humidity and hygroscopic growth covariability on model predicted AOD and PW relationships is

138   evaluated.

139   **2.1 Data Description:**

140   **2.1.1 AERONET AOD**

141   AERONET is a global ground-based network of sun photometers that measure direct sun and sky radiances over a

142   range of wavelengths (340-1640nm). These measurements are used to generate column-integrated aerosol properties

143   of AOD and aerosol microphysical and radiative properties (Holben et al. 1998; Giles et al., 2019). The network

144   includes over 600 sites with data available at https://aeronet.gsfc.nasa.gov/. The uncertainty in AERONET AOD is

145   reported to be ~0.01–0.02 for level 2 data with the higher uncertainty of 0.02 pertaining to the UV wavelengths and

146   the lower ~0.01 uncertainty associated with visible and near infrared wavelengths (Eck et al., 1999). Due to this low

147   uncertainty, AERONET AOD observations are used for validation of satellite retrievals (Remer et al. 2002, Ichoku et

148   al. 2002, Kahn et al. 2005) as well as for verification of model forecasts (Zhang et al. 2008. , Benedetti et al. 2008,

149   Sessions et al. 2015, Xian et al. 2019). For this analysis, AERONET version 3 (Giles et al. 2019), level 2 daily-

150   averaged AOD observations are used. AERONET AOD observations at 675nm for all available sites were collected

151   and sites that had a minimum of 100 daily-averaged values were retained for the analysis, with seasonal data counts

152   in Figure 2. The 675nm wavelength was selected as it is a core AERONET wavelength that is available at all sites and

153   provides parity for both the fine and coarse aerosol modes.

154
155 **2.1.2 AERONET Water Vapor**

156 Precipitable water vapor (PW), a measure of the total amount of water vapor contained in a vertical column from the
157 surface to the top of the atmosphere, is retrieved from AERONET direct sun irradiance measurements in the water
158 vapor absorption band around 940nm. The uncertainty of AERONET water vapor data is reported at 12% (Sano et al.
159 2003) and more recently, an analysis of uncertainty against radiosonde, microwave radiometry, and GPS data indicated
160 a dry bias of 5-6 % and a total estimated uncertainty of 12-15% (Perez-Ramirez et al. (2014)). The Perez-Ramirez et
161 al. (2014) evaluation with the identified uncertainty range of 12-15% included PW retrieval comparison at 3 sites
162 located in the tropics, mid-latitudes and the arctic, covering a range of climatic conditions and temperature/water vapor
163 profiles, and therefore, provides a reasonable uncertainty estimate for the entire AERONET network. The PW data
164 used in this analysis comes from the same AERONET version 3, level 2 daily-averaged dataset that is used for the
165 AOD data. As was the case for the AERONET AOD data, sites that had a minimum of 100 daily-averaged values
166 were retained for the analysis (Figure 2).

167
168 **2.1.3 NAAPS Reanalysis**

169 The NAAPS aerosol reanalysis v1.0 (Lynch et al. 2016) is a standardized global modal AOD product generated by
170 the U.S. Naval Research Laboratory (NRL) that extends over a 16 year time period (2003-2019). The core of the
171 aerosol reanalysis is the NAAPS offline aerosol transport model and its associated 2-dimensional variational data
172 assimilation system, the Navy Variational Data Assimilation System for Aerosol Optical Depth (NAVDAS-AOD).
173 NAAPS has been run semi-operationally at NRL since 1998 and became operational at the Fleet Numerical
174 Meteorology and Oceanography Center (FNMOC) in 2006 with NAVDAS-AOD operationally implemented in 2010.
175 For the NAAPS-RA, NAVDAS-AOD is used to assimilate quality-assured and quality-controlled AOD retrievals
176 from the Moderate Resolution Imaging Spectroradiometer (MODIS) and Multi-angle Imaging SpectroRadiometer
177 (MISR).

178
179 NAAPS generates 3-dimensional forecasts of dust, smoke, sea salt and a combined anthropogenic/biogenic fine
180 aerosol (ABF, also referred to in this work as pollution) mass concentration fields and the associated 3-dimensional
181 aerosol extinction and column-integrated AOD fields. As on offline model, NAAPS is driven by meteorological fields
182 from the Navy Global Environmental Model (NAVGEM) (Hogan et al. 2014), using analysis fields every 6 hours and
183 forecasts provided at 3 hour intervals. The NAVGEM analysis fields are generated using NAVDAS for assimilation
184 of a large number of conventional and satellite-based observations (Daley and Barker, 2001). NAVGEM variables
185 used by NAAPS includes the topography, sea ice, snow cover, surface stress, surface heat/moisture fluxes,
186 precipitation, lifting condensation level, cloud cover and height as well as 3-dimensional winds, temperature, and the
187 most relevant for this work, humidity. For the NAAPS analysis, aerosol sources, including dust and smoke, and
188 deposition processes were regionally tuned to best match observations (AERONET, MODIS). A detailed description
189 of the NAAPS-RA v1.0 is described in Lynch et al. 2016.

190

Atmospheric
Chemistry
and Physics
Discussions

191   In NAAPS, the Hanel (1976) formulation of the hygroscopic growth factor (f) for a given species i and relative

192   humidity (r) is used to represent the effect of humidity on particle light scattering, defined as:

193   $$f_i(r) = \left[\frac{(1-r)}{(1-r_o)}\right]^{-\gamma_i},\qquad(1)$$

194   where γ_i is an empirical species-dependent exponent (ABF=0.5 assuming 40% sulfate and 60% organics, smoke=0.18,

195   sea salt = 0.46, dust=0) and r_o is the reference relative humidity of 30%. The hygroscopic growth factor is applied

196   when calculating the aerosol scattering coefficient. In order to assess the impact of hygroscopic growth on model-

197   predicted AOD and PW correlations, a "dry" AOD is also calculated for the NAAPS-RA in which the hygroscopic

198   growth factor is not applied.

199   For this work, the NAAPS-RA v1.0 AOD fields and the NAVGEM humidity fields used in generating the NAAPS-

200   RA are extracted for the full 16 year dataset (2003-2019). NAVGEM humidity fields were integrated vertically to

201   generate model-predicted PW fields and both the PW and AOD fields were averaged on a daily basis. Additionally,

202   "dry" AOD fields were calculated for the NAAPS-RA and likewise, averaged on a daily basis.

203   **2.2 AOD and PW Relationship Analysis:**

204   **2.2.1 Correlation Analysis**

205   As a first step in understanding the relationship between aerosol and water vapor in the AERONET data record,

206   correlations (Pearson correlation coefficients) are calculated at each AERONET site with a minimum of 100 data

207   points. The correlations are calculated between the daily-averaged AOD (675nm) and PW datasets seasonally

208   (December-January-February (DJF), March-April-May (MAM), June-July-August (JJA), September-October-

209   November (SON)). This analysis is used to identify when and where relationships exist between AOD and PW in the

210   data record and the strength of the relationship. In order to provide global context to the AERONET AOD and PW

211   correlations, the same analysis was conducted using the NAAPS 16-year v1.0 reanalysis dataset. The seasonal

212   reanalysis correlations were calculated in a similar manner as the AERONET data, using daily-averaged model-

213   generated AOD and PW values. The model-generated values were then compared against observationally generated

214   AERONET correlations. The correlations in both the AERONET and NAAPS-RA evaluation were tested for

215   statistical significance at the 95% confidence level.

216   **2.2.2. Slope Evaluation**

217   In addition to the AOD and PW Pearson correlation coefficients calculated from the AERONET and NAAPS-RA

218   datasets, the slopes of the AOD and PW relationship were calculated from the seasonal data using a Theil-Sen

219   regression. A Theil-Sen regression is a robust method for fitting a line to sample points by choosing the median of

220   slopes of all lines through pairs of points. Due to the use of the median slope, the Theil-Sen method is insensitive to

221   outliers and therefore, a useful method for this analysis. With the Theil-Sen regression, a 95 % confidence interval of

222   the Theil-Sen slope was calculated for each location and season.

223   **2.2.3 Evaluation of the AOD and PW Probability Distribution**

224 In addition to a correlation and slope analysis, the AOD and PW probability distributions were also evaluated. Given
225 the expectation that aerosol and water vapor relationships will change depending on the air mass, seasonal correlations
226 can obscure the presence of aerosol and water vapor relationships when air masses with an existing relationship
227 between aerosol and water vapor occur infrequently. In this evaluation, the PW distribution associated with high AOD
228 events, defined as having an AOD value greater than 1 standard deviation above the mean, were compared to the PW
229 distribution for all data for a given location and season. A t-test was conducted to identify statistically significant
230 differences in the PW distribution means for the high AOD events and all data (p-value = 0.05). This analysis was
231 conducted seasonally (DJF, MAM, JJA, SON) using both the AERONET and the NAAPS-RA datasets.

2.2.4 Vertical Evaluation of the AOD and PW Relationship

233 While the global and AERONET site AOD and PW evaluations as well as the studies cited in the introduction provide
234 an understanding of the column-integrated relationship between aerosol and water vapor, an additional evaluation was
235 conducted to look at the aerosol and water vapor relationship in different levels of the troposphere. This evaluation
236 was conducted using the NAAPS-RA fields only, since observations of joint aerosol and water vapor vertical structure
237 are limited. Model generated correlations were calculated for a defined boundary layer (BL), lower free troposphere
238 (LT), mid-free troposphere (MT), and upper free troposphere (UT) region. The reanalysis total aerosol extinction and
239 specific humidity were vertically integrated in the first 1km of the atmosphere as a representation of the boundary
240 layer. Integration levels in the free troposphere were selected based on the sensitivities of the upper, mid-level, and
241 lower-level geostationary water vapor channels on the NOAA Geostationary Operational Environmental Satellite
242 (GOES) Advanced Baseline Imager (ABI) and the JMA Advanced Himawari Imager (AHI) with a goal of using these
243 water vapor channels to further explore aerosol and water vapor relationships in future work. The selected integration
244 levels were from 800 to 500 hPa (LT), 600 to 300 hPa (MT), and 400 to 300 hPa (UT), respectively. The vertically
245 integrated relationships, as was done for the full column-integrated evaluation, are calculated seasonally and are used
246 to identify if the model correlations are controlled by aerosol and water vapor in certain parts of the atmosphere. While
247 the boundary layer is expected to be a dominant control of the signal, given the sources of both aerosol and water
248 vapor are within the boundary layer, strong correlations within the free troposphere could indicate aerosol and water
249 vapor relationships as a result of lifting from the surface or long-range transport which typically occurs within the free
250 troposphere.

2.2.5 Impact of Hygroscopic Growth on AOD and PW relationships

252 It is well documented in the literature that water uptake on aerosol particles under moist conditions impacts aerosol
253 optical properties. Because of this, it is necessary to understand how much hygroscopic growth impacts AOD and PW
254 relationships through covariability of PW and relative humidity. The data to evaluate this observationally is not
255 available, therefore, the NAAPS-RA is used to evaluate the impact of the hygroscopic growth factor on model
256 predicted correlations. As a first step in this evaluation, the correlation between PW and relative humidity was
257 calculated by season for the previously defined vertical components of the atmosphere (boundary layer,
258 lower/mid/upper free troposphere). In order to calculate relative humidity for each defined part of the troposphere, a
259 saturation specific humidity was calculated in each model level using the reanalysis pressure and temperature fields

260   as input. Both the specific humidity and the saturation specific humidity were vertically integrated over the defined

261   levels and the ratio of the two values was used to produce a relative humidity that conserves the amount of water vapor

262   through the associated portion of the troposphere. This analysis gives a first look at where the covariability between

263   PW and RH is expected to be most impactful on the AOD and PW relationship. However, given aerosol hygroscopic

264   growth is dependent on aerosol type, the analysis was taken a step further by calculating the seasonal relationships,

265   including correlations/slopes and the probability distribution evaluation, between dry AOD and PW. The dry AOD,

266   in which the impact of hygroscopic growth on AOD is removed as described in the NAAPS-RA section (2.1.3), was

267   calculated for the full dataset. The relationships using the dry AOD are compared to the standard AOD/PW results as

268   a means to evaluate the impact of hygroscopic growth on the modeled AOD and PW relationships.

269   **2.2.6 Evaluation at Individual AERONET Sites**

270   While the previous analyses provide a global perspective on the aerosol and water vapor relationships, the relationships

271   were also evaluated at select AERONET sites to provide a first look at what is driving the observed covariability

272   between AOD and PW on an event level. The AERONET sites, including Tallahassee, Florida in the Southeast United

273   States, Beijing, China in East Asia, Izana, Canary Islands off the coast of Africa, and Alta Floresta, Brazil in South

274   America, are selected based on the strength of the observed/modeled relationships and cases are selected for different

275   seasons that exhibited both positive and negative relationships. While this evaluation does not by any means provide

276   a complete understanding of the drivers of these relationships across the globe, it can be used to provide some insight.

277   **3.0 Results**

278   This study is highly multi-dimensional. In order to elucidate the findings, the results are first presented as a global

279   evaluation, which is followed by a more in-depth discussion by region, level, and accounting for the impacts of

280   hygroscopicity. As aerosol regimes are typically seasonal in nature, all evaluations are performed for DJF-MAM-JJA-

281   SON. Summaries of the data used in the analyses are presented in Figures 2 through 6, including: Figure 2, seasonal

282   counts of daily-averaged AERONET AOD and PW data; Figure 3, seasonal mean AERONET and NAAPS-RA AOD

283   and PW values; Figure 4 seasonal NAAPS-RA AOD averages by aerosol types (dust, sea salt, anthropogenic/biogenic

284   fine, biomass burning); and Figures 5 and 6, the NAAPS-RA AOD and PW (respectively) 25th, 75th, and 90th

285   percentiles from daily data and associated interquartile range (IQR) of by season. In regards to the AERONET

286   analysis, only sites with a minimum of 100 data points are included, as previously discussed. Due to this constraint,

287   some temporary sites used for field campaigns are excluded in this work.

288   **3.1 Global Patterns of AOD-PW Correlation**

289   Overall, the seasonal patterns in both AOD and PW are pretty consistent between AERONET and the NAAPS-RA

290   (Figure 3). For example, peak AOD values in North America and Europe occur during the summer months in both

291   datasets. Likewise, peak AOD values are found over the Sahel in winter and spring due to a combination of dry-season

292   biomass burning and dust associated with the northeasterly Harmattan winds with shifts in peak AOD further north in

293   summer due to increased dust activity over the Sahara. Like the Sahel, peak AOD values associated with fire activity

294   during regional dry seasons are also found in both datasets for Central and South America, Southern Africa and

Atmospheric
Chemistry
and Physics
Discussions

295 Southeast Asia. Boreal regions, which also exhibit seasonality due to fires in summer months, are not as well sampled
296 in the AERONET dataset, making it harder to see seasonal shifts in AOD. However, this seasonality is found in the
297 NAAPS-RA. Likewise, northward shifts in PW are seen in AERONET and the NAAPS-RA in the summer and a
298 southward shift in the winter months. A more in-depth discussion of the data by region is below:

299 1) North America: The largest number of AERONET sites are present in this region with ~180 included in the
300 analysis. AERONET data counts are the highest in the summer months (JJA) which also coincides with
301 peak mean AOD and PW values in both the AERONET and NAAPS-RA datasets (Figure 3). Summertime
302 peak AOD values are associated with ABF and smoke aerosol types, concentrated to the North, and a
303 combination of ABF and transported dust to the South (Figure 4). Despite JJA being associated with the
304 highest AOD values, the IQR is only around 0.1-0.2 (Figure 5). The 90th percentile AOD values in JJA for
305 North America are mainly associated with large smoke events, particularly originating from the Pacific
306 Northwest and Boreal regions (Figure 5). High AOD values are also observed in MAM months concentrated
307 in the Southeast United States (Figures 2 and 5), associated with smoke (originating from Central American
308 fires) and ABF/pollution aerosol types (Figure 5).

309 2) Europe: Data from ~125 AERONET sites was included in the analysis in Europe. Like the North America
310 region, peak AERONET data counts occur during JJA months (Figure 2). Peak AOD values are observed
311 during MAM and JJA (Figures 3 and 5), mainly associated with pollution in Eastern Europe, and
312 Mediterranean dust (Figure 4). PW values also peak during JJA (Figures 2 and 6). AOD IQR values, like
313 North America, are relatively small and on the order of 0.1-0.2 in JJA/MAM, with 90th percentile AOD
314 events in the 0.3-0.5 range.

315 3) East Asia: The analysis in East Asia included data from ~52 AERONET sites. AERONET data counts are
316 relatively consistent throughout the seasons (Figure 2). AOD values in East Asia are high throughout the year
317 due to the presence of pollution, concentrated to the East and dust, particularly in the spring and summer
318 (Figure 4). While pollution aerosol is present throughout the year, AOD values tend to be higher in the winter
319 months than the summer months in the NAAPS-RA (Figures 3 and 5) with the strength of the East Asian
320 Monsoon being a controlling factor in the spatial distribution and aerosol concentration in the region (Zhang
321 et al. 2010; Yan et al. 2011; Zhu et al. 2012; Mao and Liao, 2017). However, in the AERONET dataset, the
322 highest AOD values are observed in the summer months, consistent with the literature (Eck et al. 2005, 2018).
323 This discrepancy may be related to the satellite data that is assimilated in the NAAPS-RA in the summer
324 months. High AOD values are often misclassified as cloudy by the retrieval algorithms and subsequently
325 screened (Eck et al. 2018), which can contribute to low AOD biases in the model (Reid et al. 2022). The
326 range in AOD values is particularly large over East Asia as shown by the percentiles in Figure 5 with peak
327 IQR values of around 0.6-0.7 occurring during DJF.

328 4) South America: Data from ~44 AERONET sites was used in the analysis in South America. AERONET
329 data counts are the greatest during JJA and SON months, which is coincident with the highest AOD values.
330 This is particularly the case in SON, which is the dry season in South America when fire activity is increased.

331   The dominance of smoke aerosol is shown in the NAAPS-RA for these months (Figure 4). Extreme event
332   AOD values (90th percentile) and the IQR are the greatest for SON, again due to fire activity (Figure 5).

333   5)   Northern Africa: Data from ~39 sites were used for evaluation in Northern Africa. Data counts are relatively
334   consistent across the seasons with the exception of the Banizoumbou, Niger site with approximately 1600
335   data points from 16 years of data during the DJF season. The AERONET and reanalysis average AOD values
336   for the North African Sahel region peaks in the winter and spring months (DJF, MAM) due to a combination
337   of dust and smoke aerosol (Figure 4). Peak Sahel AOD values coincide with the ITCZ being its most southern
338   position, which is shown in the PW fields (Figure 3 and 6). North Africa, particularly the Sahara, has high
339   AOD in the spring and summer months due to dust outbreaks with peak AOD values exceeding 1 and IQR
340   values in the 0.4-0.5 range (Figure 5).

341   6)   Southern Africa: The analysis in Southern Africa included data from ~30 AERONET sites. AERONET data
342   counts are pretty consistent throughout the year, however, there are less sites available for analysis during
343   the DJF months. AOD values in Southern Africa are the highest in JJA and SON which is coincident with
344   peak fire activity in the region.

345   7)   Arabian Peninsula: AERONET data counts from ~20 sites are consistent across the seasons in this region.
346   While dust emissions are present through the year, peak dust activity occurs in the summer months as shown
347   in the AERONET and NAAPS-RA AOD mean and percentile values (Figures 3 and 5).

348   8)   India: The number of AERONET sites was ~20 in India with locations concentrated towards the North for
349   sampling the Indo Gangetic Plain in which pollution dominated AOD is present throughout the year, with
350   peak AOD values exceeding 1 during all seasons (Figure 3-5). Dust aerosol from the Thar Desert and the
351   Arabian Peninsula are transported to western India, particularly in the MAM and JJA seasons, while smoke
352   aerosol contributes to AOD in eastern India in MAM. AOD and PW are heavily influenced by the summer
353   monsoon season in which peak PW is observed (Figures 3 and 6).

354   9)   Southeast Asia: Data from ~21 sites was available for the analysis in Southeast Asia. The number sites used
355   is greatest in the spring (Figure 2), coincident with the Peninsular Southeast Asia fire season in which peak
356   AOD values exceed 1 and large IQR values are present (Figure 5). Peak AOD values shift towards Insular
357   Southeast Asia during the SON months in which fire activity increases. Pollution is also present throughout
358   the year.

359   Regressions of AOD and PW for the daily data by season, including correlation coefficients and slopes, and the
360   statistically significant difference in mean PW between the distribution associated with high AOD events only and the
361   full PW distribution for both the NAAPS-RA and AERONET daily data are presented in Figure 7 with confidence
362   intervals on the Theil-Sen slopes shown in Figure 8. Red regions/sites indicate a positive correlation in which higher
363   PW is associated with higher AOD values and blue regions indicate a negative relationship in which lower PW is
364   associated with high AOD values. For all evaluations in Figure 7, the predominant signal is positive (ie. red) in both
365   the AERONET observations and the NAAPS-RA with the strongest correlations varying by season, and/or aerosol
366   regime. In the AERONET dataset, the strongest positive correlations are summarized in Tables 1-4 for DJF, MAM,
367   JJA, and SON, respectively. Also included are NAAPS-RA values for these sites as a means of comparison. For winter

368   months (DJF), the strongest positive correlations (>0.6) occur at sites in the Southeast United States, East Asia and
369   select sites in the Middle East such as Dhadnah, UAE (Table 1). In the spring months (MAM), dominant positive
370   relationships occur at mostly Eastern United States sites and the Nainital site in India (Table 2). Southern Africa sites
371   associated with smoke aerosol, Eastern European sites, and select sites in the Eastern United States have the strongest
372   positive correlations in the summer months (JJA) (Table 3, Figure 7). In the fall (SON), AERONET positive
373   correlations are strongest for the Eastern United States, select European sites as well as a site at Dhadnah, United Arab
374   Emirates.

375   The NAAPS-RA daily correlations (Figure 7) within seasonal aggregates indicate similar but not identical spatial
376   patterns relative to the AERONET dataset. The dominant positive correlation regions include the Eastern/Southeastern
377   United States as is found in AERONET. Likewise, stronger European AOD and PW correlations are found in the
378   summer months, in Eastern Asia in the winter season, and the Middle East in the fall. The NAAPS-RA results are
379   helpful in that it provides a more complete perspective on the AOD and PW relationships. In addition to strong positive
380   correlations in Southeast United States and East Asia during DJF, the NAAPS-RA also indicates strong positive
381   correlations in parts of Southwest Asia (Iran/Afghanistan/Pakistan), India, South America, and Southern Africa, which
382   are minimally if not at all sampled by AERONET. The spatial extent of the observationally-sampled relationships can
383   also be seen. For example in MAM, the AERONET correlation at the Tamanrasset site in Algeria is 0.55 with a
384   consistent NAAPS-RA correlation of 0.53. In the reanalysis, the correlations, greater than 0.5, extend to the east of
385   Tamanrasset. Likewise, the spatial extent of correlations for maritime regions can be seen in the reanalysis, where
386   AERONET sites are rare. In JJA months, correlations at the Dahkla site in Morocco are 0.45 in the AERONET dataset.
387   Although the NAAPS-RA correlation at Dahkla is weaker (R=0.31), the positive relationship observed in both datasets
388   on the West coast of Africa can be seen extending out into the Atlantic ocean in the reanalysis, consistent with dust
389   transport pathways. Correlations associated with aerosol transport are also seen in Southern Africa in the reanalysis,
390   extending out into the ocean.

391   Although positive correlations are dominant throughout the world, negative correlations were also identified in both
392   the AERONET and NAAPS-RA datasets from daily data. In the AERONET dataset, negative correlations are limited
393   to the tropic/subtropics with negatively correlated regions mostly associated with biomass burning. The strongest
394   negative correlations in the AERONET dataset are shown in Tables 1-4 with NAAPS-RA values shown for
395   comparison. During all seasons, negative correlations are found in the Sahel region in both AERONET and the
396   NAAPS-RA with the negative relationships extending further northwards in the spring and summer months. This
397   results in an exceptionally strong dipole between Saharan and Sahelian outflow and is likely related to shifts in the
398   ITCZ. This points to aerosol sources (biomass burning and dust) and scavenging as a cause of the negative AOD and
399   PW relationship. The NAAPS-RA shows these negative correlations extending into the Atlantic Ocean with seasonally
400   dependent differences. Negative correlations extend into the Caribbean in JJA and to northern parts of South America
401   in MAM, consistent with seasonal transport pathways. Other negative correlation regions include Southeast Asia,
402   South America, and Southern Africa. For these regions, the strongest negative correlations are associated with the
403   respective dry, burning seasons. For example, negative correlations are strongest in Peninsular Southeast Asia in

404   MAM and in Insular Southeast Asia and South America in SON. In these cases, negative AOD and PW relationships

405   are likely a result of higher aerosol emission occurring under dry conditions, which lead to more fire activity. Southern

406   Africa is an exception during JJA, in which smoke aerosol is dominant (Figure 4). However, this is consistent with

407   previous studies which have found elevated free tropospheric water vapor levels associated with Southern African

408   smoke events (Adebiyi et al. 2015; Pistone et al. 2021). Correlations in both AERONET and the NAAPS-RA are

409   positive in JJA and negative in MAM and SON when smoke aerosol is also present, but not at its peak. One of the

410   largest AERONET negative correlations occurs at the Jomsom, Nepal site in JJA with a value of -0.65 (Table 3),

411   although nearby sites show small or statistically insignificant correlations. The Jomson site is located at 2825 meters

412   with maximum PW values around 2 while the nearby Pokhara site is 2000 meters lower in altitude with maximum

413   PW values around 5, therefore, Jomson is likely a regional outlier due to altitude effects. For Jomsom and the

414   surrounding regions, the NAAPS-RA indicates no statistically significant correlation. While NAAPS and AERONET

415   are in general agreement in the locations of negative correlations, this discrepancy is likely related to meso or small

416   scale features that are not captured in a global, 1 degree model.

417

418   **3.2 Consistency between AERONET and NAAPS-RA**

419   While the global plots of AERONET and NAAPS-RA AOD and PW relationships give a sense of spatial agreement,

420   a scatterplot comparison of the quantitative values generated from the two datasets are used to take a closer look at

421   the consistency between the observed and predicted relationships. A seasonal comparison of AERONET and NAAPS-

422   RA regressions is shown as a scatterplot in Figure 9, including site by site a) correlations; b) Theil-Sen slopes; and c)

423   the PW mean difference for high AOD events. In addition to the three scatterplot comparisons, all locations for which

424   for the sign of the AOD and PW relationships differed between the AERONET and the NAAPS-RA datasets were

425   identified. For these identified sites, the distribution of AERONET correlations are plotted by season in Figure 9d.

426   This is included as a means to examine the strength of the observed AOD/PW relationship under conditions when the

427   datasets disagree. Overall, the observations and model are in general agreement in the sign of the correlations (Figure

428   9a) with similar results found for the Theil-Sen slope and the PW mean differences for high AOD events (Figure 9b,c).

429   Differences in the sign of the correlation are found for 15.5, 9.5, 10.2, 10.1% of analyzed AERONET sites for the

430   DJF, MAM, JJA, and SON months, respectively. For all seasons except JJA, these differences are mostly associated

431   with a negative correlation in the AERONET data and a positive value in the NAAPS-RA. Differences in correlation

432   sign occur for sites in which the AERONET-generated correlations are weak, mostly falling below 0.20 (Figure 9d),

433   with the exception of the Jomson AERONET site in JJA in which AERONET indicated a strong negative correlation

434   and the reanalysis had a slight positive, but statistically insignificant relationship as previously discussed. For the

435   strongest correlation sites, AERONET and NAAPS are in good agreement in DJF and MAM (Tables 1 and 2). For

436   JJA and SON, NAAPS-RA has a tendency to produce weaker correlations relative to AERONET (Tables 3 and 4).

437   Some differences are expected given that the event sampling is different between the AERONET observations and

438   the 16-year NAAPS-RA. However, the overall agreement in the correlations between the two datasets provides some

439   confidence in the NAAPS-RA for generating regionally and seasonally varying AOD and PW relationships on a global

440   scale.

3.3 Slope Evaluation

With the consistency between AERONET and NAAPS-RA established, a more thorough evaluation of the strength of the slope of AOD-PW relationship has been conducted. As previously discussed, the AOD and PW relationship in both the AERONET and NAAPS-RA datasets were quantified using a Theil-Sen regression in order to fit a slope to the change in AOD per unit cm PW (Figures 7 and 8). Examples of NAAPS-RA and AERONET Theil-Sen fittings for eight AERONET sites scattered over the globe, each with their own unique aerosol environment are shown in Figure 10. Included are positive and negative correlation examples shown for each season (DJF: Beijing China and Lamto, Ivory Coast; MAM-Houston Texas and Ilorin Nigeria; JJA-Helsinki, Finland and Dakar Senagal; and SON-Dhadnah UAE and Palangkaraya, Indonesia) with the selected sites having some of the strongest correlations for the respective seasons in the AERONET and NAAPS-RA datasets (Tables 1-4). Good agreement is shown between the NAAPS-RA and AERONET-generated Theil-Sen slopes at the selected sites with the largest differences occurring at the Lamto and Palangkaraya sites in which relatively less AERONET observations are available. These fittings are calculated for each grid and AERONET site and are used to generate the results in Figures 7 and 8. The examples in Figure 10 show the insensitivity of the Theil-Sen regression to outliers, while the correlation coefficient is quite sensitive to such values. Beijing in DJF exhibits a large change in AOD with PW, as high AOD events are more frequent at this location (Figures 5 and 10). However, places like Houston, Helsinki and Dhadnah have relatively smaller Theil-Sen slopes as high AOD events, with a value around 1, occur less frequently and do not influence the slope. For these locations, the range of frequently observed AOD events is much smaller (Figures 5 and 10), resulting in small changes in AOD with PW. Although there is certainly scatter in the data points in Figure 10, statistically significant trends exist. The scatter in the data points occurs more so at negative correlation locations (Figure 10), resulting in smaller correlation coefficients. While the relationships for both positive and negatively correlated locations are statistically significant and the Theil-Sen regression gives an overall trend, the scatter indicates differences in AOD and PW relationships will occur from day to day. This is expected as the AOD-PW relationship is based on a combination of transport covariance and local meteorology-source relationships.

The global and seasonal pattern in the positive and negative Theil-Sen slopes are consistent with the correlation analysis results (Figures 7 and 8). The biggest Theil-Sen slopes tend to occur where larger IQR ranges are present (Figure 5), as was shown for the Beijing Theil-Sen slope example in Figure 10. The largest slopes in both datasets are centered on Beijing in the DJF months with values exceeding $1 cm^{-1}$. Beijing consistently has some of the largest positive changes in AOD with PW in the AERONET dataset for all seasons with values, including 95% confidence intervals, of 1.1(1.0-1.2), 0.35(0.32-0.38), 0.46(0.43-0.51), and 0.26(0.22-0.3) cm-1 for DJF, MAM, JJA, and SON, respectively. The NAAPS-RA is largely consistent with AERONET for the DJF and MAM months with corresponding values of 1.13(1.08-1.18), and 0.31(0.29-0.33) cm-1. Less sensitivity to PW is found in the reanalysis for JJA and SON with corresponding values at Beijing of 0.13(.11-0.14), and 0.18 (0.17-0.20) cm-1. This is likely due to an underestimation of haze formation within NAAPS, as with other global models (e.g., Sessions et al., 2015; Xian et al., 2019) and also possibly due to the underestimation of AOD in summer from NAAPS due to a low AOD bias in the assimilated satellite AOD datasets in the East Asia region (Eck et al., 2018). Large positive changes in AOD with PW extend through Asia, the Middle East, and Northern Africa, all regions impacted by high AOD events. As is the case

478   in the correlation results, the strong dipole in slopes is clear over North Africa with positive slopes to the North and

479   negative slopes in the southern Sahel region. Likewise, negative slopes are mainly associated with burning regions

480   with the exception of Southern Africa in JJA. Statistically significant correlations and slopes at high latitudes,

481   particularly Antarctica, indicate aerosol/water vapor transport in the model since local sources are limited, although

482   AOD and PW values are low (Figures 5 and 6).

483   Recall the scatterplot comparison of AERONET and NAAPS generated changes in AOD with PW is shown in Figure

484   9(b). Again, there is generally good agreement between the datasets, consistent with the correlation comparison. The

485   signs of the slopes are the same with the exception of 14.6, 9.2, 12.3, and 8.1% of sites for DJF, MAM, JJA, and SON,

486   respectively. Sites where differences in sign are observed have weak correlations (Figure 8d). The NAAPS-RA has a

487   tendency to under-predict negative changes in AOD with PW relative to AERONET for SON months where peak

488   negative slopes are generated from AERONET. This is also shown in Table 4 as well as the global maps in Figure 7

489   where differences can be seen, particularly in the Sahel and Southeast Asia. At the Kuching site in Borneo in SON,

490   the AERONET generated slope is -0.37(-0.48 to -0.28) cm-1 with a reanalysis value of -0.11(-0.13 to -0.09) cm-1

491   likely due to strong mesoscale variability and poor constraint in biomass burning on Borneo (Reid et al., 2013; Wang

492   et al., 2013). Additionally, this could again be due to satellite retrieval screening of smoke as cloud and NAAPS failing

493   to simulate the highest AOD smoke events in Borneo, especially in the dry El Nino years such as 2015 (Eck et al.

494   2019, Shi et al. 2019). The reanalysis also tends to under predict positive slopes for JJA at the AERONET sites where

495   the largest slopes are observed. This difference is not restricted to a particular region, but can be seen in East Asia,

496   Africa, and Mexico City (Figure 7). As an example, the Tamanrasset site in Algeria exhibits slopes in the AERONET

497   data of 0.26(0.23-0.30) cm-1 and in the reanalysis of 0.07(0.06-0.08). Likewise, at the Lubango site in Angola, the

498   slope is 0.27(0.21-0.34) cm-1 in the AERONET data and 0.13(0.12-0.14) cm-1 in the reanalysis. The Tamanrasset

499   site is at 1377 meters altitude in the Ahaggar Mountains which is significantly higher than the surrounding terrain in

500   the Saharan Desert. The Lubango site in Angola is at 2047 meters, also higher than a portion of the surrounding terrain.

501   This terrain/altitude influence is likely a factor in the discrepancies. The differences in slopes for JJA are also shown

502   in Table 3.

3.4 Evaluation of the AOD and PW Probability Distribution

504   While the correlation and slope evaluation is used to define a seasonal AOD and PW relationship across the datasets,

505   it is expected that variations in the aerosol and water vapor relationship will exist across air masses. As a result, a

506   probability distribution evaluation is another useful way to examine the data. The seasonal evaluation of the probability

507   distributions is included in Figure 7, below the correlation and slope results. The plots show the statistically significant

508   difference in the mean for the PW distribution associated with high AOD events (AOD values more than 1 standard

509   deviation above the mean) and the full PW distribution. Red regions/sites indicate that the PW mean for high AOD

510   events is statistically higher than the full distribution mean (i.e. higher moisture levels). Blue regions/sites indicate a

511   lower PW mean for high AOD events (i.e. dryer conditions). Regions or sites in white have no statistically significant

512   difference. The spatial pattern in the probability distribution evaluation are similar to the correlation and slope analysis,

513   however, the probability distribution evaluation highlights different regions than the previous analyses. For example,

514 across all seasons, larger changes in PW for high AOD events are observed in Argentina, South America, including

515 at the CEILAP-BA (Buenos Aires, Argentina) with values of 0.88, 0.94, 1.01, and 1.00 cm for DJF, MAM, JJA, SON

516 in the AERONET dataset and values of 0.61, 0.35, 0.95, and 0.73 cm in the NAAPS-RA dataset. This is a region that

517 is impacted by both local pollution and transported biomass burning (Resquin et al. 2018). Larger changes in PW for

518 high AOD events are also observed over Northern Australia during MAM, which is consistent with peak bushfire

519 season in the region. Larger changes in PW are also found over the United States and Canada, consistent with patterns

520 in the correlation evaluation, but with more pronounced values relative to other locations. ABF is generally the

521 dominant aerosol type with biomass burning from Central America and Western US/Boreal Regions during the MAM

522 and JJA seasons, respectively. Likewise, Eurasian Boreal regions associated with biomass burning activity during JJA

523 are more pronounced in the PW distribution evaluation. The peak in values in the Southeast United States are found

524 during the DJF season. During MAM and SON, the peak areas include most of the Eastern United States and extending

525 into Canada and Central America. However, regions that were more pronounced in the correlation and slope

526 evaluation, have smaller differences in mean PW for high AOD events, Beijing being a good example of this. Based

527 on AERONET, the difference in mean PW at Beijing is 0.21cm while the difference is 0.35cm in the NAAPS-RA for

528 DJF when the strongest correlations and largest slopes were found. However, sites like Stennis, Mississippi (Table 1)

529 which had a much smaller slope than Beijing ($0.04cm^{-1}$ compared to $1.1cm^{-1}$) have a much larger difference in mean

530 PW with the AERONET value of 1.08cm and the NAAPS value of 1.16cm. This is because the probability distribution

531 evaluation is taking into account those infrequent, outlier events that don't affect the Theil-Sen slopes. Locations

532 where the IQR is relatively small, such as the United States, Europe, Australia, and parts of South America and

533 Southern Africa have greater differences in mean PW, despite having small Theil-Sen slopes, due to the impact of

534 outlier events. For many of these regions, the outliers are associated with biomass burning, indicating that PW is a

535 useful tracer for such events.

536 Like the correlation and slope evaluation, a comparison of AERONET and NAAPS generated differences in mean

537 PW was conducted by season. Similar to the previous two comparisons, AERONET and NAAPS are in agreement in

538 the sign of PW difference for most locations, demonstrated by the global plots in Figure 7 and the scatterplots in

539 Figure 8c. The % of sites that have differences in sign between the two datasets are 8.9, 6.87, 5.86, and 4.15% for

540 DJF, MAM, JJA, and SON, respectively. These percentages are smaller than the % of sites with differences in the

541 correlation and slope analysis. However, like the previous evaluations, most sites that exhibit sign differences between

542 AERONET and NAAPS had weak AOD and PW relationships (R<0.20, Figure 8d), with the exception of some

543 outliers in which small scale features that cannot be resolved in the global model may be at play. The comparisons

544 between AERONET and NAAPS-RA across the different evaluations indicate that NAAPS is generating AOD and

545 PW relationships that are pretty consistent with the observational data. Although differences in magnitude are present,

546 the direction of the relationships are very consistent, providing confidence in the use of the NAAPS-RA for further

547 exploring the AOD and PW relationship, particularly in the vertical and accounting for hygroscopic affects.

548 **3.5 Vertical Evaluation of the AOD and PW Relationship**

549   In addition to calculating the full column-integrated AOD and PW correlations in the NAAPS-RA, the correlations
550   were also evaluated by vertically integrating the extinction and specific humidity through previously defined pressure
551   levels in the atmosphere that correspond to a boundary layer, lower, middle, and upper free troposphere. This
552   evaluation was conducted seasonally, like the fully integrated analysis, with results shown in Figure 11. In addition to
553   the global plots, histograms of the AOD and PW correlations for the full column and the vertical components of the
554   atmosphere are shown in Figure 12. It is notable that stronger positive correlations exist when looking at limited parts
555   of the atmosphere compared to the fully integrated column. This is most evident in the global plots for ocean regions,
556   particularly in the Southern Hemisphere, where correlations exceeding 0.5 occur compared to the fully integrated
557   correlations that are on the order of 0.2. This result is not unexpected given that the vertical components of the
558   atmosphere look different depending on things like vertical mixing, a local aerosol and water vapor source compared
559   to a long-range transport event, the relative humidity profile etc. Additionally, some regions exhibit stronger
560   correlations in certain portions of the atmosphere. For example, dust dominated regions such as the Sahara, Arabian
561   Peninsula and the Gobi and Taklimakan deserts have the strongest correlations in the mid FT. This is higher up in the
562   atmosphere than expected, given for example, studies have shown East Asian dust heights to range from 1.9 to 3.1km
563   (Liu et al. 2019) and the typical description of the Saharan Air Layer (SAL) includes dust-laden air between
564   approximately 850 and 500 hPa (Karyampudi et al. 1999) with several other studies identifying Saharan dust up to
565   ~5km for summertime dust transport (Mortier et al. 2016, Veselovskii et al. 2016, Tesche et al. 2011). This indicates
566   that the model may be transporting too much dust aerosol and water vapor higher into the atmosphere and this transport
567   is well correlated. Correlations over North America and Eastern Europe are strongest in the BL to lower FT.
568   Wintertime correlations over East Asia/Beijing are pretty consistent throughout the column. Negative correlation
569   regions associated with smoke aerosol, including the Sahel, Southern Africa, and Southeast Asia have the strongest
570   correlations in the lower FT and largely disappear beyond this point. The shift in correlations with vertical location
571   are also evident in the histograms (Figure 12) when compared to the full column distribution. This is particularly the
572   case for the lower and mid free troposphere where the number of grids with correlations greater than 0.5 increase.
573   Additionally, the shift of the correlations to mostly positive can be seen in the mid and upper free troposphere
574   histograms.

575   **3.6 Impact of Hygroscopic Growth on AOD and PW relationships**
576   The final consideration in this work is hygroscopicity. Although the effects of clouds on the AOD and PW relationship
577   is also important to understand, this effect cannot be investigated using NAAPS since the model does not account for
578   the processing of aerosol in cloud droplet, rapid gas-to-particle conversion in cloud droplets or the high RH halo in
579   the immediate vicinity of clouds. However, this should be considered in follow-on work. While relationships between
580   AOD and PW have been demonstrated, this signal can be either from co-transport or a confounding relationship
581   between enhanced PW and RH. The correlation between RH and PW is shown in Figure 13 by season and for the
582   boundary layer and parts of the free troposphere. The largest spatial variations in the PW and RH correlation occur in
583   the boundary layer, as anticipated, with strong correlations found over Africa, extending into the Indian Ocean/India,
584   located further North during JJA and further South during DJF and similar patterns during MAM and SON. Other
585   regions of high correlation in the boundary layer include off the coast of South America, parts of Australia, and limited

586 locations in the tropical oceans. Beyond the boundary layer, the overall patterns are generally consistent throughout
587 the vertical column with strong correlations in the subtropics and tropics (>0.9) with some variations on the extent by
588 season. In JJA for example, this high correlation region extends further north while in DJF the high correlation region
589 extends further in the Southern hemisphere. In this highly correlated region, hygroscopic growth is expected to be a
590 significant driver in AOD and PW relationships when dust is not the dominant aerosol type. RH and PW correlations
591 are higher over ocean regions than over land in the northern hemisphere, which should be impactful for sea salt aerosol
592 and PW correlations. The impact of the RH and PW correlations on the AOD and PW relationship are shown in
593 calculated seasonal relationships between "dry" AOD, which excludes the impact of hygroscopic growth, and PW in
594 the NAAPS-RA in Figure 14. This figure includes the correlations, the slope of the "dry" AOD and PW relationship,
595 and the statistically significant different in mean PW for high "dry" AOD events. The removal of hygroscopic growth
596 from the AOD calculation had the following outcomes on the resulting correlations: 1) the previously positive
597 correlation was reduced in magnitude 2) the previously negative correlation coefficient became more negative 3) the
598 sign of the correlation flipped from positive to negative and 4) little to no change in the correlation. Regions such as
599 the Eastern United States and Europe fall into the first category where positive AOD and PW correlations are found
600 for all seasons, but the correlation coefficient is greatly reduced. For the Eastern United States, peak correlation
601 coefficients were in the approximately 0.6-0.7 range with hygroscopic growth and fell below 0.5 without it. This is
602 especially true in JJA when RH and PW correlations are the strongest. Likewise, positive correlations in Europe are
603 still present, but weakened. In these cases, hygroscopic growth amplifies an existing positive relationship that is
604 somewhat weak when evaluating seasonal data by correlation. In regards to the second category, this corresponds to
605 regions dominated by smoke aerosol that previously exhibited negative AOD and PW relationships, such as Peninsular
606 Southeast Asia during the MAM months and Insular Southeast Asia during the SON months. Additionally, increases
607 in negative correlations are found for aerosol transport from Asia across the Pacific Ocean. In these cases, hygroscopic
608 growth reduces an existing negative relationship between aerosol and water vapor. Ocean regions mostly account for
609 the third category where the correlation flipped from a weak positive to negative value. Regions that are dominated
610 by dust, including the Sahara and Arabian Peninsula, fell into the fourth category as there is no hygroscopic growth
611 for dust in NAAPS.
612
613 In regards to the slope of "dry" AOD and PW, the same categories apply with similar spatial patterns relative to the
614 correlation analysis. Additionally, the same is true when examining the difference in mean PW for high "dry" AOD
615 cases. In this case, it is found that either: 1) an increase in PW is still statistically significant, but the difference in
616 mean PW is much less 2) a decrease in PW for high "dry" AOD cases is still statistically significant with a larger
617 decrease when not considering hygroscopic growth 3) the sign of the difference flipped from an increase in PW to a
618 decrease or the difference became statistically insignificant and 4) the PW difference did not change much due to dust
619 dominated conditions. While the modeled differences in PW are statistically significant when excluding hygroscopic
620 growth, they are small, with peak differences on the order of a few millimeters. The results here indicate that
621 hygroscopic growth of aerosol plays an important role in the AOD and PW relationship. While PW is still a good
622 tracer for AOD as shown in this work, it should be kept in mind that there is a difference in water vapor as a tracer for

623   AOD and for aerosol mass. It is expected that the relationship between "dry" AOD and PW would be a closer

624   representation of the dry aerosol mass to PW relationship.

3.7 Discussion through Example Cases at Individual AERONET Sites

626   In order to further understand regional differences in observed AOD and PW relationships, individual sites in which

627   strong AOD and PW relationships were identified and had several years of observational data available were selected

628   for further analysis. These sites included: 1) Tallahassee, Florida for Southeast US pollution (Figure 15); 2) Beijing,

629   China for Asian haze and dust (Figure 16); 3) Izana, Canary Islands for Saharan dust (Figure 17); and Alta Floresta,

630   Brazil for South American biomass burning (Figure 18). For the four identified AERONET sites, the daily-averaged

631   AOD and PW timeseries are examined for seasons in which correlations were found to be strong. This includes DJF

632   for the Tallahassee and Beijing sites and JJA for Izana. At these sites, the identified relationships between AOD and

633   PW were positive. The Alta Floresta site, which exhibited negative AOD and PW relationships in the presented results,

634   is further examined for the SON biomass burning season. The daily-averaged data are included since this is what was

635   analyzed in the previous analyses. Additionally, the AERONET data, without any averaging, is further examined for

636   individual cases from the site-specific timeseries for which peaks in AOD and/or PW were found. NAAPS-RA AOD

637   and PW fields are also shown for the selected cases (Figures 15-18).

638   At the Tallahassee site, the predominant aerosol type is ABF/pollution and although AOD values are generally low

639   during DJF (mean values in the 0.1-0.2 range, Figure 3), strong AOD and PW relationships were found with

640   correlations of 0.74 in the AERONET dataset and 0.66 in the NAAPS-RA with PW mean differences around 1cm for

641   high AOD events (Table 1). The daily-averaged AOD and PW timeseries for the 2018-2019 DJF season are shown in

642   Figure 15a. The timeseries indicates, consistent with the correlation analysis, that the daily-average AOD and PW

643   generally move together. There are several joint peaks in AOD and PW that occur during the time period and three

644   selected cases are examined further, including 1/1/2019, 2/7/2019, and 2/17/2019, with these events identified in the

645   Figure15a timeseries using red arrows. The AERONET AOD and PW timeseries for these three cases are shown in

646   Figures 15b-d, respectively. The 2/17 case has the least data points available, making it harder to evaluate diurnal

647   changes in AOD and PW, however, the 1/1 and 2/7 cases have a good number of data points throughout the afternoon

648   and later into the evening. For these two cases in particular, the changes in AOD and PW throughout the day are

649   generally consistent with each other, indicating that the AOD and PW relationships can extend to sub-daily timescales.

650   AOD and PW plots for the three identified cases are shown from the NAAPS-RA in Figure 15e as a means to assess

651   the types of aerosol events that are impacting Tallahassee when coordinated peaks in AOD and PW are observed. For

652   all three cases, coincident transport of AOD and PW is observed in the reanalysis fields, associated with a frontal

653   system. This type of frontal transport was commonly found for events in which coincident PW and AOD peaks are

654   observed at Tallahassee. As the DJF season in the Southeast United States has significant frontal activity, this is likely

655   an important factor in enhanced AOD/PW relationships during this season.

656   Beijing is an urban site that commonly experiences high AOD levels related to pollution as well as transported dust

657   and smoke events. Wintertime events are notorious for exhibiting some of the worst air quality in the world for a major

658   population center (e.g., Wang et al., 2014; Gao et al., 2016; Zhang et al., 2018). Additionally, Beijing has the benefit

Atmospheric
Chemistry
and Physics
Discussions

Open Access

EGU

659   of a long AERONET data record with measurements dating back to 2001. Like Tallahassee, the AOD and PW

660   timeseries at Beijing is evaluated for the 2018-2019 DJF season (Figure 16) with strong positive relationships

661   identified in both the AERONET and NAAPS datasets with correlations of 0.71 and 0.76, respectively, and the change

662   in AOD with PW exceeding 1cm^{-1} (Table 1). As indicated in Figure 4, ABF/pollution is the dominant aerosol type

663   with some dust present with much higher AOD values observed at this location (Figures 3 and 5). In East Asia,

664   pollution build-up often occurs under stagnant weather conditions where a stable atmosphere leads to limited vertical

665   mixing (Wang et al. 2014, Li et al. 2019) with the monsoon being an important factor in determining synoptic

666   conditions. In particular, the East Asian Winter Monsoon (EAWM) has been shown to be a controlling factor in aerosol

667   concentrations during the winter season (Li et al. 2016; Jeong et al. 2017). With a strong EAWM, reduced aerosol

668   concentration occur over northern East Asia, including Beijing, due to stronger northerly winds. In weaker EAWM

669   years, increased aerosol concentrations occur in the north due to weakened winds and more stagnant conditions. The

670   daily-averaged AERONET AOD and PW timeseries for 2018-2019 DJF is shown in Figure 16a. Consistent with the

671   previously presented evaluations, the daily-average time series for this particular DJF time period are well correlated

672   with AOD and PW moving up and down together. As was done for the Tallahassee site, several peaks in AOD and

673   PW were selected for further evaluation and are highlighted with red arrows on Figure 16a, including the peak on 1/3

674   and its subsequent decrease on 1/4/19, and the peak on 12/20/18 and its subsequent decrease on 12/21/18. The non-

675   averaged AERONET AOD and PW timeseries for these two cases are shown in Figure 16b and c, respectively, with

676   a zoomed in view of 12/21 on Figure 16d. For both of these events, high AOD from ABF/pollution and PW values

677   are observed with a subsequent dropoff the following day, which are well coordinated in the full dataset. The closer

678   look at the data on 12/21/18 (16d), like the previous Tallahassee examples, shows consistent movement between the

679   measured AOD and PW indicating the presence of correlations on short timescales. For both of these events, the

680   NAAPS-RA AOD and PW fields are shown for both the peak and subsequent dropoff in Figure 16e. The movement

681   of the large-scale air mass can be seen in both the AOD and PW fields. For the 1/3/19-1/4/19 event, NAVGEM

682   meteorological fields indicate weakened northerly winds due to a region of high pressure over the eastern portion of

683   the continent, leading to stagnant conditions at the surface in Beijing and local pollution and water vapor build-up. On

684   the following day, the high pressure system moved eastward. As a result, the Siberian High northerlies were no longer

685   suppressed and a more typical wintertime circulation resumes with the winds jointly pushing the aerosol and water

686   vapor southward and away from Beijing. For the 12/20/18-12/21/18 case, extensive multi-level cloud cover can be

687   seen in both MODIS Terra and Aqua images on 12/20, indicating that this may be a case where clouds may have

688   played a role in gas-to-particle conversion in the polluted air and/or enhanced particle humidification in the high RH

689   fields associated the clouds, consistent with the findings of Eck et al. (2018). As the air mass moves on 12/21, a joint

690   reduction in both AOD and PW is observed at Beijing, demonstrating the impact of large scale transport. Thus in the

691   Beijing case, the overall regional weather patterns are an important factor in the AOD and PW relationship.

692

693   The third site that is examined is Izana in the Canary Islands (Figure 17). The Izana site, which is located

694   approximately 300km west of the African coast, is particularly useful for evaluating aerosol and water vapor

695   relationships for free tropospheric dust. It has also been noted in the community that against a Saharan air layer free

Atmospheric
Chemistry
and Physics
Discussions

Open Access

EGU

696   subsidence regime, the infrared signals of Saharan Air Layer dust are quite small relative to co-transported water vapor
697   (Gutleben et al., 2019; Ryder, 2021: Barreto et al., 2022). Nevertheless, forecasters find the water vapor signal useful
698   in tracking dust events (Kuciauskas et al., 2018). Izana is a mountain site located at approximately 2400m, above a
699   strong subtropical temperature inversion layer which makes it ideal for monitoring free tropospheric plumes. In the
700   summer months, frequent and intense Saharan air mass outbreaks in the subtropical free troposphere impact the site.
701   Particularly large AOD dust storms were observed transporting Saharan dust across the Atlantic in the summer of
702   2020, including the so called "Godzilla" dust event in June that has been examined in detail in previous studies (Francis
703   et al. 2020). As a result, this time period was evaluated in further detail at Izana with a focus on several dust events.
704   In the analysis conducted in this work, positive relationships between AOD and PW were found in both the AERONET
705   and NAAPS datasets at Izana during the JJA season with the AERONET dataset having a correlation of 0.66 and the
706   NAAPS-RA indicating a weaker correlation of 0.48 (Table 3). As noted for other sites, this difference may be due to
707   altitude effects at the Izana site which may not be captured in NAAPS. The daily-average AOD and PW timeseries
708   for the 2020 JJA season at Izana are shown in Figure 17a. The AOD and PW are pretty well correlated, although there
709   are PW peaks present without the presence of aerosol. As sources of aerosol and water vapor are different, this is not
710   unexpected. Three of the peak from the timeseries as indicated by the red arrows were selected for further evaluation,
711   including 6/14/20, 7/18/20, and 7/31/20 with timeseries shown in Figures 17b-d, respectively. As was shown for the
712   previous pollution cases, the AOD and PW are well correlated in the non-averaged dataset showing the presence of
713   correlations for dust events on timescales less than a day. The NAAPS-RA AOD and PW fields are shown for the
714   6/14/20 case in addition to the associated dropoff of both AOD and PW on 6/18/20, as well as for the 7/18/20 and
715   7/31/20 events in Figure 17e. For the 6/14/20 case, CALIPSO indicates dust tops near Izana at around 5km. A cutoff
716   low was present to the northwest of Africa and a subtropical high over the Western coast of Africa which resulted in
717   increased dust generation and recirculation. The southwesterly winds transport the dust to Izana on June 14 and at the
718   same time, moist ocean air shown by the PW fields is transported to Izana as well, resulting in a spike in both AOD
719   and PW at the AERONET site. On June 18, the moisture and dust begin pushing south and west across the Atlantic,
720   resulting in decreases in AOD and PW at the same time at Izana. Similar examples of dust and water vapor cotransport
721   are shown for the 7/18/20 and 7/31/20 cases. These results are consistent with previous studies which have indicated
722   enhanced water vapor mixing ratios associated with the dust in Saharan Air Layer events (Marsham et al. 2008, Jung
723   et al. 2013, Kanitz et al. 2014). Thus, Izana is a good example of subtropical free tropospheric co-transport of water
724   vapor and dust.

725

726   The final site evaluated was Alta Floresta, Brazil for the 2019 SON season, when biomass burning is the dominant
727   aerosol type. Here, there is a strong seasonal dependency: drier seasonal conditions are associated with a July-October
728   biomass burning season. At this site and other regions of biomass burning, negative correlations between AOD and
729   PW were identified in the presented evaluations. For Alta Floresta, SON correlations of -0.38 and –0.47 were
730   generated from the AERONET and NAAPS-RA datasets, respectively (Table 4). The daily-average AOD and PW
731   timeseries are shown in Figure 18a. An important thing to note about this timeseries is that a clear downward shift in
732   the PW fields occurs during October, consistent with monthly site climatologies from AERONET (3.61cm in

733   September, 4.15cm in October, 4.5cm in November). As fires are associated with dry conditions, the AOD fields

734   decrease as the water vapor increases. This shift towards wetter and decreased aerosol conditions is driving the

735   seasonal negative correlations for biomass burning regions. However, despite this overall shift, peaks in AOD and PW

736   are generally positively correlated. Several such cases are highlighted in the timeseries, including 9/15/19, and 9/23/19.

737   The 9/9/19 event is also highlighted in which the daily-averaged AOD peaks and the PW is at a low. For all three

738   cases, the AOD and PW timeseries shown in Figures b-d, show good positive correlations with AOD and PW changing

739   in the same way throughout the day. For the 9/9/19 case, this appears to a more locally driven event with the extent of

740   the smoke being more limited and the air being drier than the surrounding areas, suggesting a different air mass (Figure

741   18e). Additionally, there is much more small scale variability in the AOD and PW fields (Figure 18b). For this type

742   of event, the daily-average PW fields might not be as good of an indicator of what is going on with AOD. For the

743   other two cases, the NAAPS-RA plots indicate larger spatial extent of the smoke with more moisture associated with

744   the air mass. In this case, daily-average PW is a better indicator for large scale smoke events. However, for all three

745   smoke cases, AOD and PW are correlated on an event level. Thus, in this case the AOD-PW relationship identified in

746   the previously presented AERONET and NAAPS-RA evaluations represents the end of the burning season with wet

747   season onset in the middle of a "climatological season". However, PW is a good positive indicator of AOD associated

748   with smoke on an event level, consistent with what has previously been shown in the literature for case study

749   evaluations.

750   **4.0 Conclusions and Implications**

751   The relationship between AOD and PW was evaluated globally and on seasonal and daily timescales using

752   approximately 20 years of AERONET observational data and the 16-year NAAPS-RA v1.0 model fields. As

753   AERONET observations have small measurement uncertainties, the observational analysis provides a best estimate

754   of the AOD and PW relationships. The observational analysis was combined with the NAAPS-RA in order to provide

755   a complete global perspective on the AOD and PW relationship as well as to provide an avenue for further exploration,

756   including what the likely drivers of these relationships are, what the relationships look like when taking the vertical

757   location into account, and the impact of hygroscopic growth on the AOD and PW correlations.

758   The major findings of this work include:

759   1. Seasonal relationships between AOD and PW are present across the globe at both seasonal and daily levels.

760   Most often AOD and PW relationships are strongly positive at seasonal to daily time scales, especially for

761   species such as pollution and dust. Biomass burning, however, has negative seasonal relationships due to fire

762   proclivity in dry seasons. Nevertheless, positive daily relationships are observed, associated with transport.

763   For regions like the Sahel, negative relationships between AOD and PW were found with spatial patterns

764   consistent with shifts in the ITCZ in which convection leads to aerosol scavenging.

765   2. Mid-latitude relationships between AOD and PW appear to be driven by frontal activity. While

766   tropical/subtropical relationships are driven by seasonal monsoon activity, ITCZ, and dry season patterns.

767   Dust transport associated with African easterly waves and cyclones are the link between aerosol and water
768   vapor for the Sahara.

769 3. The observed correlations between the AOD and PW were stronger when evaluated by vertical level with the
770   strongest correlations identified in the free troposphere, consistent with large scale aerosol and water vapor
771   transport. The location of the strongest correlations varied by aerosol type with dust dominated regions
772   having the strongest correlations in the mid free troposphere and smoke dominated regions having the
773   strongest correlations in the lower free troposphere.

774 4. Hygroscopic growth of aerosol particles, which is associated with increased relative humidity and often
775   occurs with increasing PW, has a large influence on the observed covariability between AOD and PW,
776   particularly in the mid-latitudes and for non-dust aerosol species. While transport covariance between AOD
777   and PW is present, the imbedded RH to PW relationship is the dominant term. This indicates that PW is a
778   good tracer for AOD, but not necessarily aerosol mass.

779 5. Covariability between AOD and PW for dust-dominated events is statistically significant and hygroscopic
780   growth is not an important factor.

781   Overall, this evaluation provides a global perspective on AOD and PW relationships. As has been previously
782   shown for individual case studies in the literature, this work reaffirms that PW is a useful tracer for aerosol
783   transport and such relationships are present across the globe. The seasonal AOD and PW evaluations conducted
784   in this work highlight regions and seasons for which AOD and PW relationships are expected to be more
785   prevalent. In particular, regions and seasons for which strong correlations and impacts on the PW distribution for
786   high AOD events are found are associated with synoptic scale aerosol events, including large-scale pollution and
787   smoke events over CONUS and Europe, Saharan dust events over the Atlantic, biomass burning events during
788   regional dry seasons in South/Central America, Africa, and Southeast Asia, and Asian dust/haze events. This is
789   confirmed when evaluating AOD and PW relationships on an event basis in different parts of the world in which
790   coincident peaks in daily-averaged AOD and PW were associated with large-scale aerosol transport events. The
791   vertical evaluation of the AOD and PW relationship provides further evidence that a strong contributor to the
792   identified relationship is synoptic scale aerosol transport in the free troposphere where the relationships were
793   found to be stronger than the fully integrated vertical column. These signals were present for all aerosol types
794   evaluated, indicating PW can be a useful tracer for AOD associated with all aerosol types as long as sources of
795   both and a common linking transport mechanism are present. For example, in the United States, fronts were the
796   linking transport mechanism while in East Asia, monsoonal patterns controlled joint transport. Likewise, dust
797   transport associated with African easterly waves and cyclones linked aerosol and water vapor for the Sahara.
798   Regions identified with strong correlations indicate the frequent presence of such synoptic scale co-transport
799   events while the PW distribution evaluation for high AOD events highlights regions in which such events are
800   present, but can be infrequent, as was the case for Boreal smoke events in summertime.

801   This work provides a first step in understanding the important aerosol and water vapor relationship on a global
802   scale. While aerosol and water vapor relationships will vary from air mass to air mass, this analysis provides an

Atmospheric
Chemistry
and Physics
Discussions

Open Access
EGU

803 understanding of where and when AOD and PW relationships are expected to be of importance and can be
804 exploited in 1) using water vapor as an aerosol tracer 2) in data assimilation applications and 3) for radiative
805 transfer studies in which collocated aerosol and water vapor can impact results. While this analysis provides a
806 quantitative estimate of the aerosol and water vapor relationship in a big picture sense, the next step is to further
807 understand the aerosol and water vapor relationships on an event level. This is particularly important for data
808 assimilation in which an understanding of how this relationship temporally and spatially evolves for individual
809 air masses needs to be developed. As such, a follow-on study will be conducted to investigate the evolution of
810 aerosol and water vapor in space and time on an event level with a focus on specific regions identified in this
811 work.

812 **Code and data availability**

813 AERONET observations are available for download through https://aeronet.gsfc.nasa.gov/ and the NAAPS
814 reanalysis data in NetCDF format can be downloaded through The US Global Ocean Data Assimilation
815 Experiment (GODAE) server (https://usgodae.org/).

816 **Author contributions**

817 Authors Juli Rubin and Jeffrey Reid planned the analysis while Juli Rubin conducted the majority of the analyses
818 presented in this work. Peng Xian provided the NAAPS-RA dataset and provided help in using the data. Jeffrey
819 Reid, Juli Rubin, Christopher Selman and Thomas Eck helped in interpreting the results of the study with Chris
820 Selman focused on the meteorological aspect and Thomas Eck providing important feedback on the evaluation
821 using AERONET data.

822 **Competing interests**

823 The peer-review process was guided by an independent editor, and the authors have no other competing interests
824 to declare.

825

826
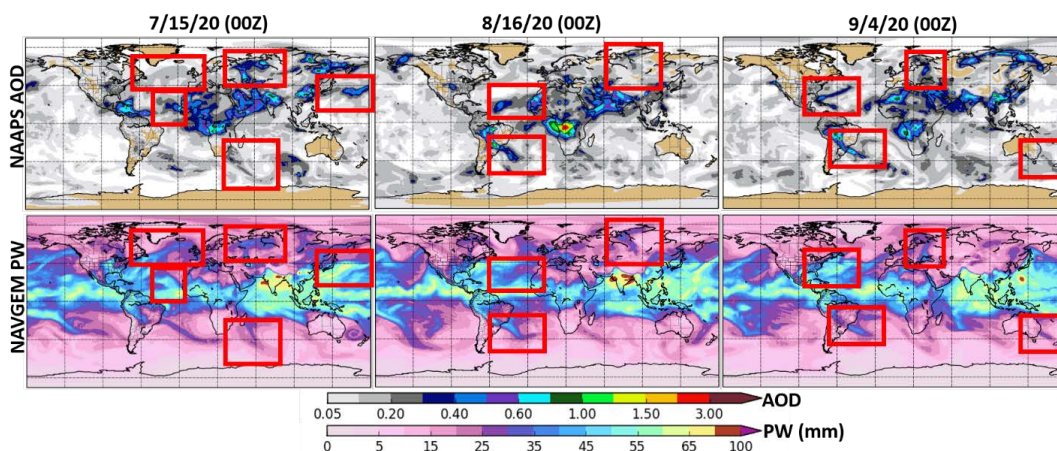
Figure 1. Examples of NAAPS AOD and NAVGEM PW forecasts in which similar synoptic scale transport patterns are found, particularly in the mid-latitudes. Aerosol and water vapor features with similar transport patterns are highlighted in matching red boxes in the AOD and PW plots. These types of co-transport events of both positive and negative correlation are found in forecasts on a daily basis.

831
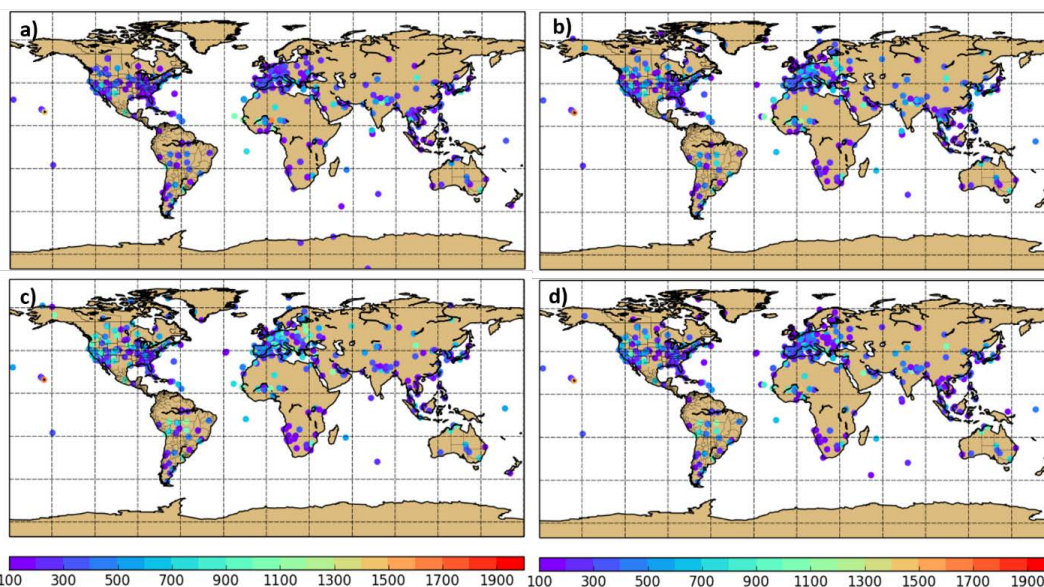
Figure 2. Count of daily-averaged AERONET AOD and PW data points by season: a) DJF b) MAM c) JJA d) SON. Only sites with at least 100 points are shown.

834

835
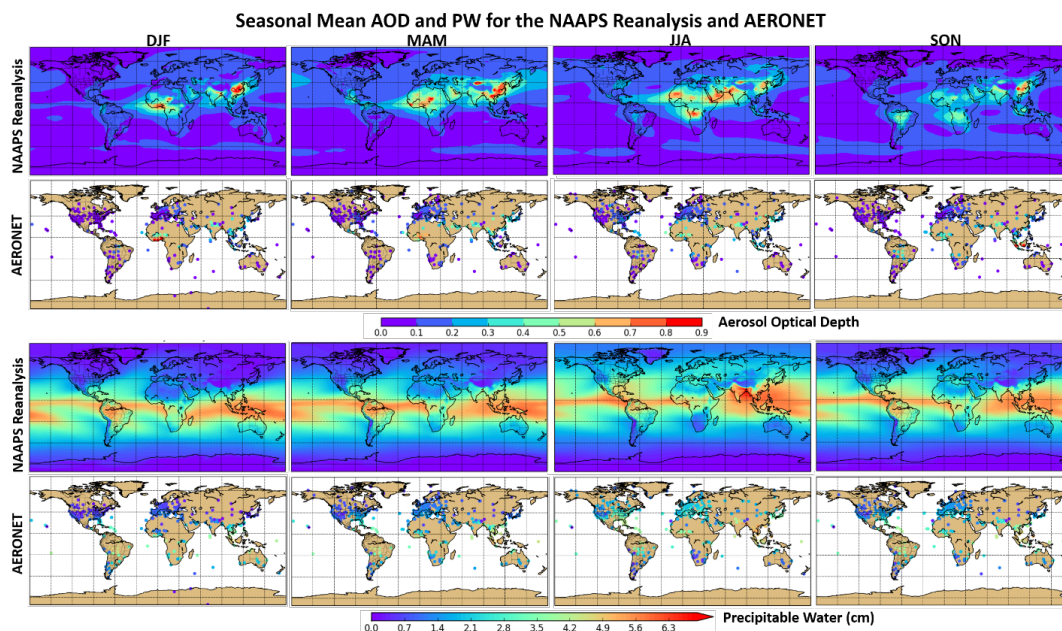
Figure 3. Mean AOD and Precipitable Water (cm) for the NAAPS-RA and at AERONET sites by season: DJF, MAM, JJA, SON.
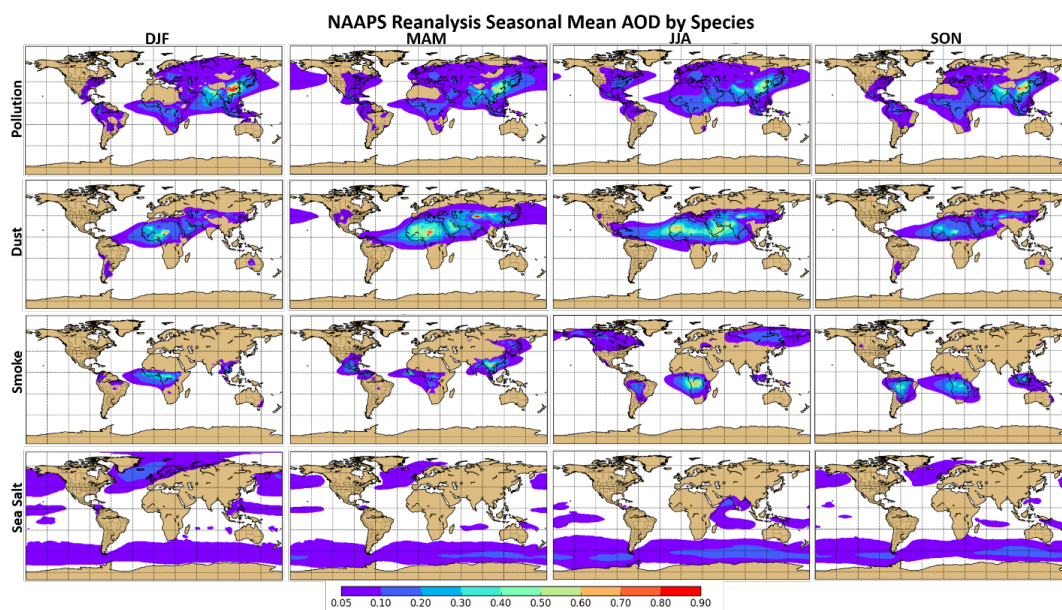
Figure 4. NAAPS-RA seasonally averaged AOD by aerosol type, including pollution (anthropogenic and biogenic fine aerosol), dust, smoke, and sea salt.

25

842
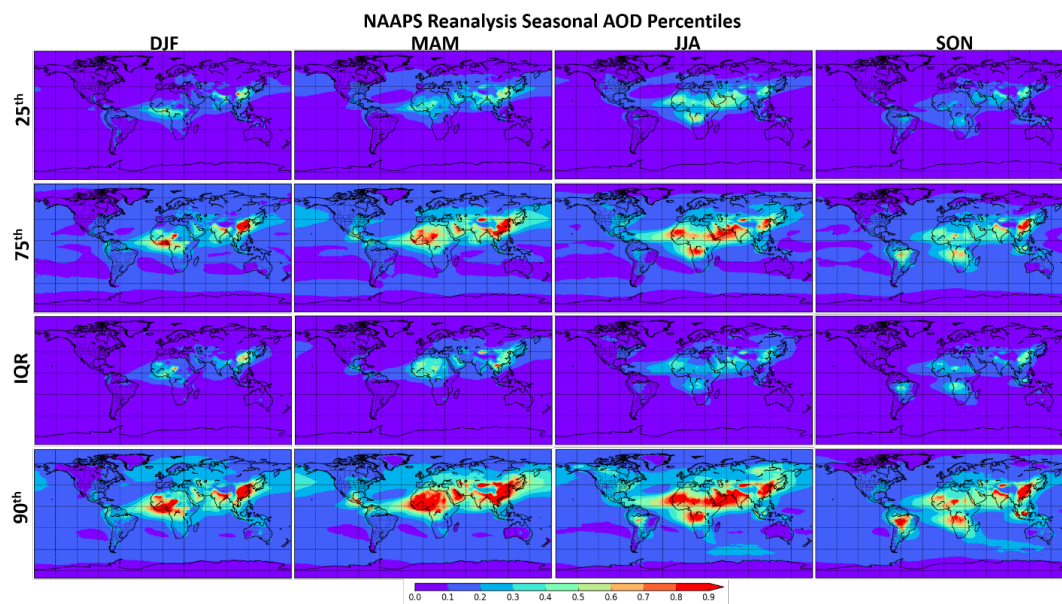
Figure 5. NAAPS-RA AOD percentiles by season (DJF, MAM, JJA, SON). The 25th and 75th percentiles are shown along
with the interquartile range (IQR). The 90th percentile is used to show high AOD values at a given location.

845

846
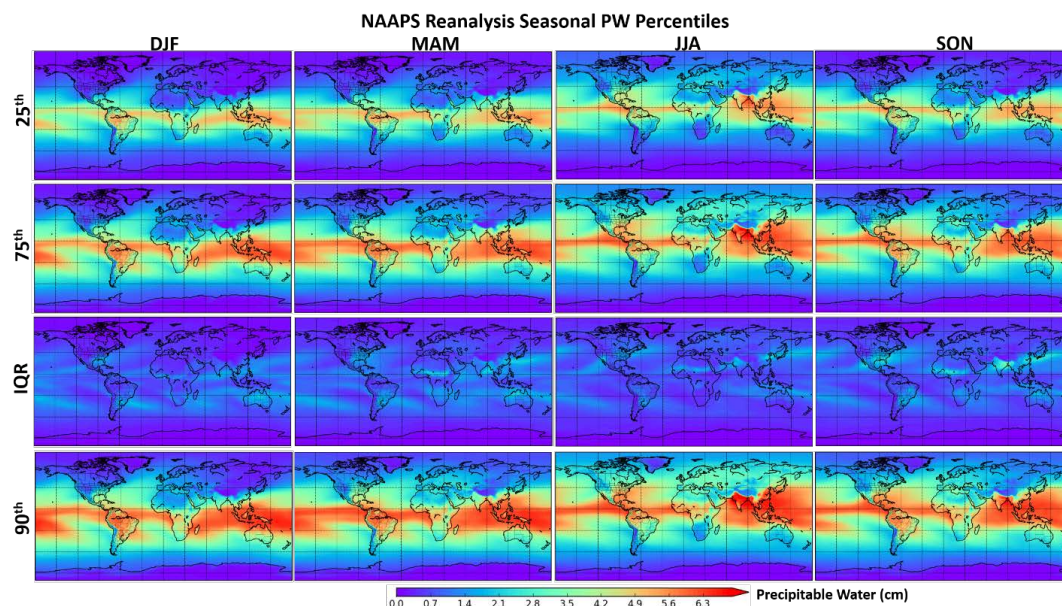
Figure 6. NAAPS-RA PW percentiles by season (DJF, MAM, JJA, SON). The 25th and 75th percentiles are shown along
with the interquartile range (IQR). The 90th percentile is used to show high PW values at a given location.

849
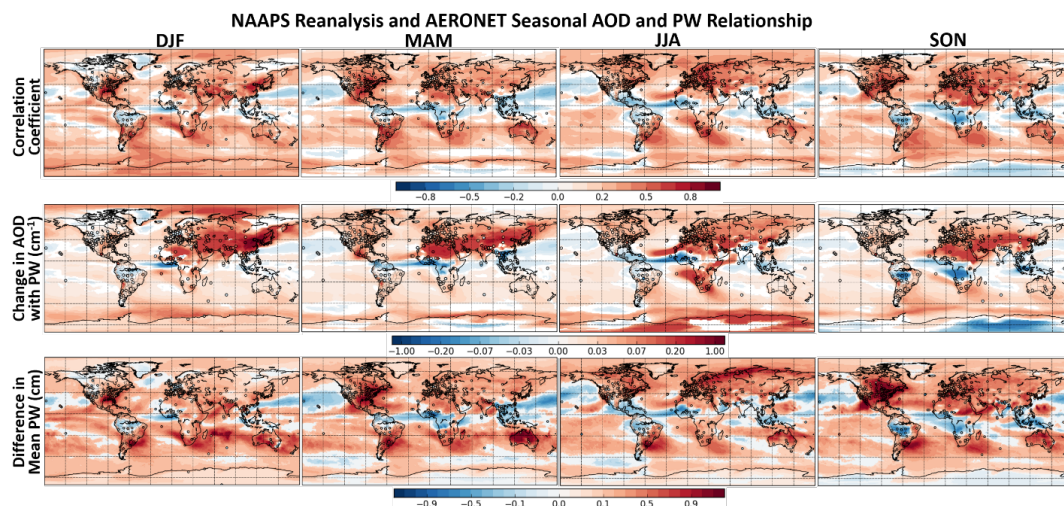
Figure 7. Seasonal AOD and PW relationships based on AERONET data (circles) and the NAAPS-RA (global map) shown as: a) correlation coefficients between daily-averaged AOD and PW (non-zero values are statistically significant at the 95% level) b) Theil-Sen regression slopes (change in AOD with PW) between daily-averaged AOD and PW in units of cm-1 at locations where the correlation is statistically significant and c) the statistically significant difference in mean PW (cm) between the PW distribution associated with high AOD events (> 1 standard deviation above mean) and the PW distribution for all AOD values. Red regions indicate a positive relationship between AOD and PW (higher moisture conditions for higher AOD events) and blue regions indicate a negative relationship (dryer conditions for higher AOD events).

857
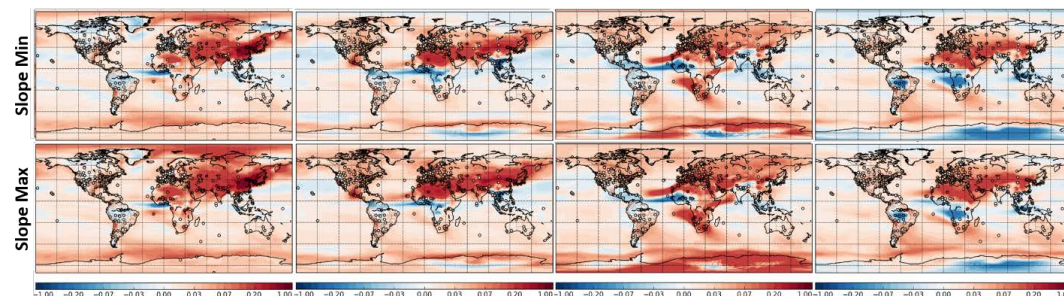
Figure 8. The 95% confidence interval in the Theil-Sen change in AOD with PW (cm-1) for DJF, MAM, JJA, and SON. The confidence intervals are shown for both the NAAPS-RA and AERONET.

860

861

862

Scatterplot Comparison of AERONET and NAAPS Seasonal AOD/PW Relationships

863
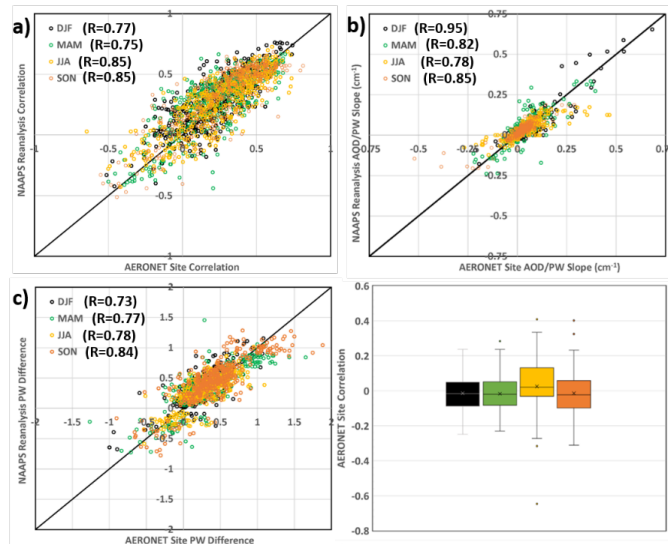
Figure 9. Scatterplot comparisons of the NAAPS-RA and AERONET: a) AOD and PW correlations at AERONET sites b)
the change in AOD with PW (cm-1) at AERONET sites and c) the statistically significant difference in mean PW associated
with high AOD events compared to the full PW distribution at AERONET sites. The comparisons are shown by season
(DJF, MAM, SON, JJA) and correlations between the datasets are included. Additionally, the distribution of AERONET
site correlations for which sign differences were found between NAAPS and AERONET calculated AOD/PW relationships
are shown seasonally in d).

870
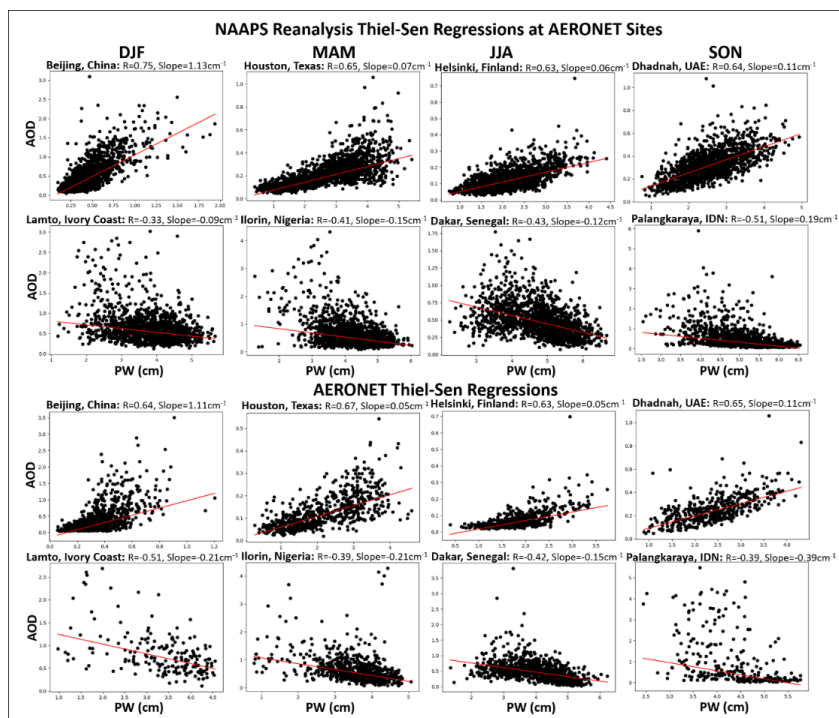
Figure 10. Seasonal examples of NAAPS-RA and AERONET Theil-Sen regression calculations for positive correlation locations (Beijing, Houston, Helsinki, Dhadnah) and a negative correlation locations (Lamto, Ilorin, Dakar, Palangkaraya). The black dots are the AOD and PW pairs from the NAAPS-RA or AERONET and the red line is the Theil-Sen fitting, which is the median of the slopes for the range of data pairings. The location name, correlation coefficient (R), and the Theil-Sen slope (Slope) are included with each plot.

Atmospheric
Chemistry
and Physics
Discussions
Open Access
EGU
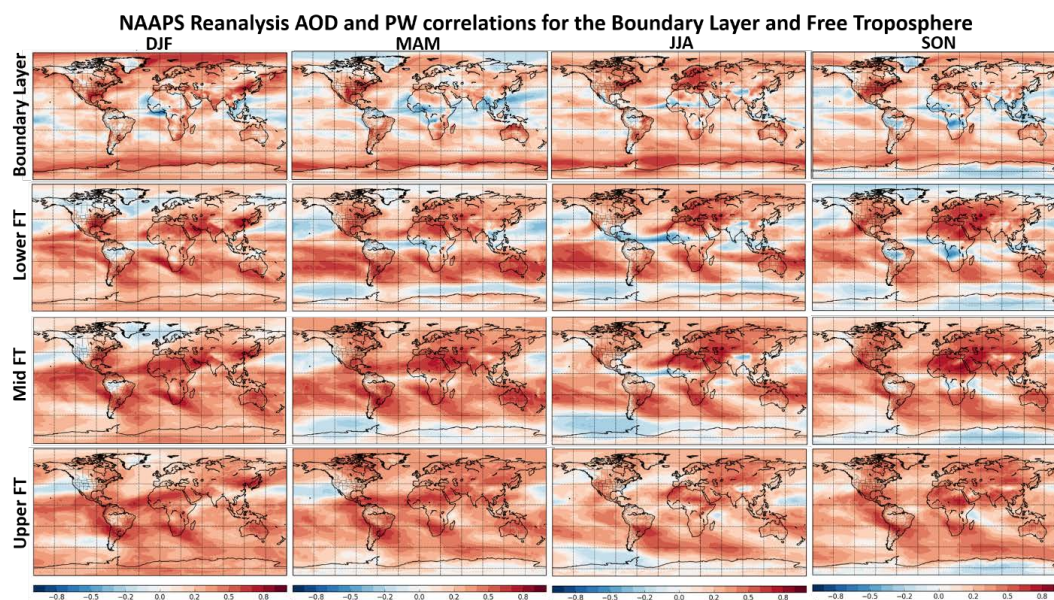
Figure 11. NAAPS-RA seasonal correlations (DJF, MAM, JJA, SON) between vertically-integrated total aerosol extinction and specific humidity in the boundary layer, lower free troposphere, mid free troposphere and upper free troposphere. Red values indicate a positive correlation and blue values indicate a negative correlation.
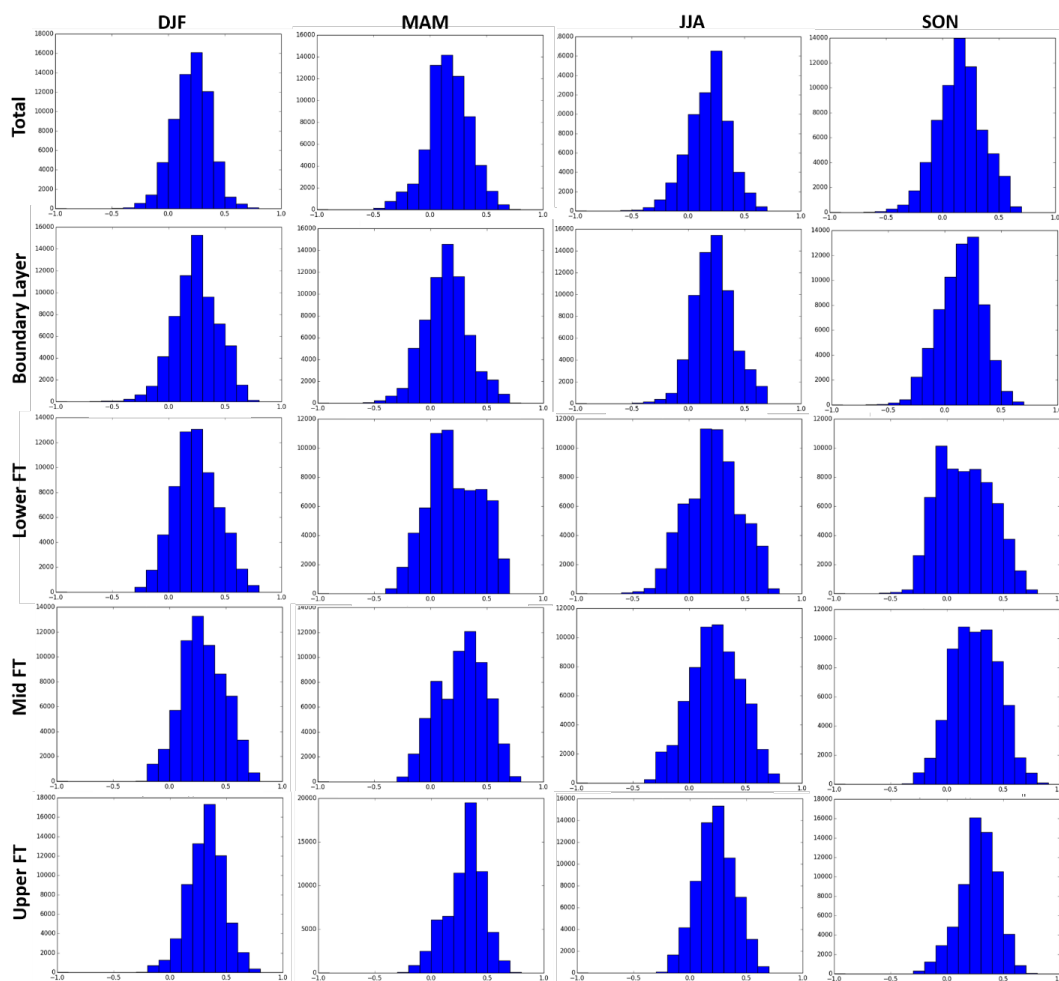
Figure 12. AOD and PW correlation histograms by season for the full integrated column (Total) and vertical components of the atmosphere (Boundary Layer, Lower/Mid/Upper Free Troposphere).

886
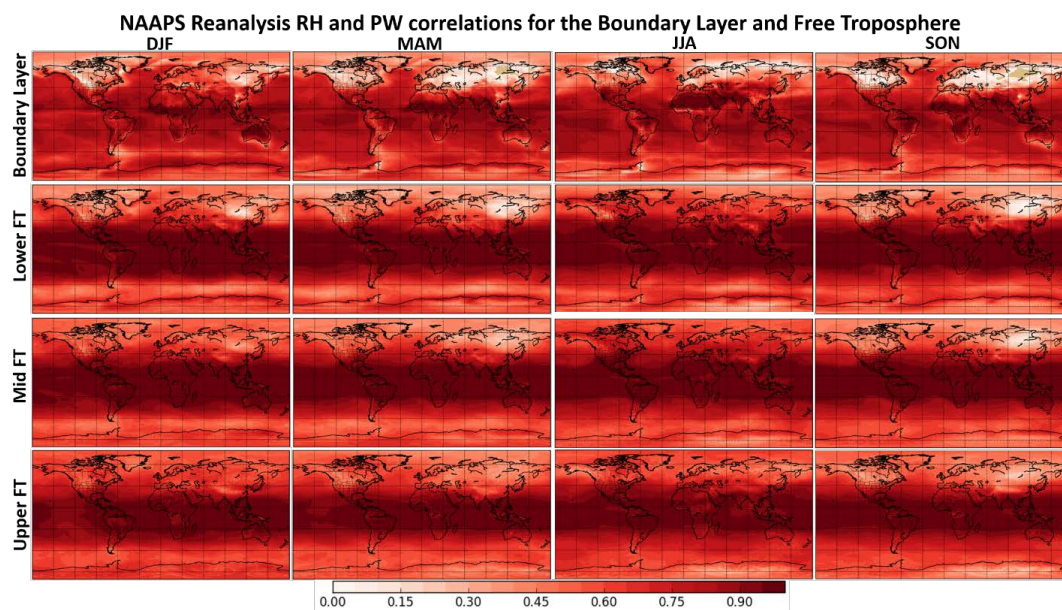
Figure 13. NAAPS-RA seasonal correlations (DJF, MAM, JJA, SON) between vertically-integrated relative humidity (integrated specific humidity/integrated saturation specific humidity) and specific humidity in the boundary layer, lower free troposphere, mid free troposphere and upper free troposphere.

890

891
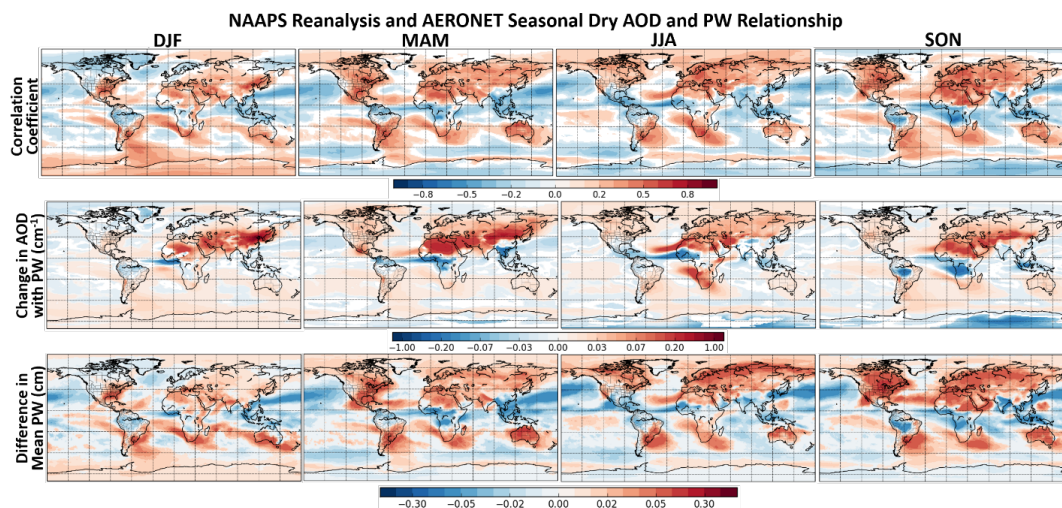
Figure 14. Seasonal dry AOD and PW relationships based on the NAAPS-RA shown as: a) correlation coefficients between daily-averaged dry AOD and PW (non-zero values are statistically significant at the 95% level) b) Theil-Sen regression slopes (change in AOD with PW) between daily-averaged dry AOD and PW in units of cm-1 at locations where the correlation is statistically significant and c) the statistically significant difference in mean PW (cm) between the PW distribution associated with high dry AOD events (> 1 standard deviation above mean) and the PW distribution for all AOD

897   values. Red regions indicate a positive relationship between dry AOD and PW and blue regions indicate a negative
898   relationship.

899
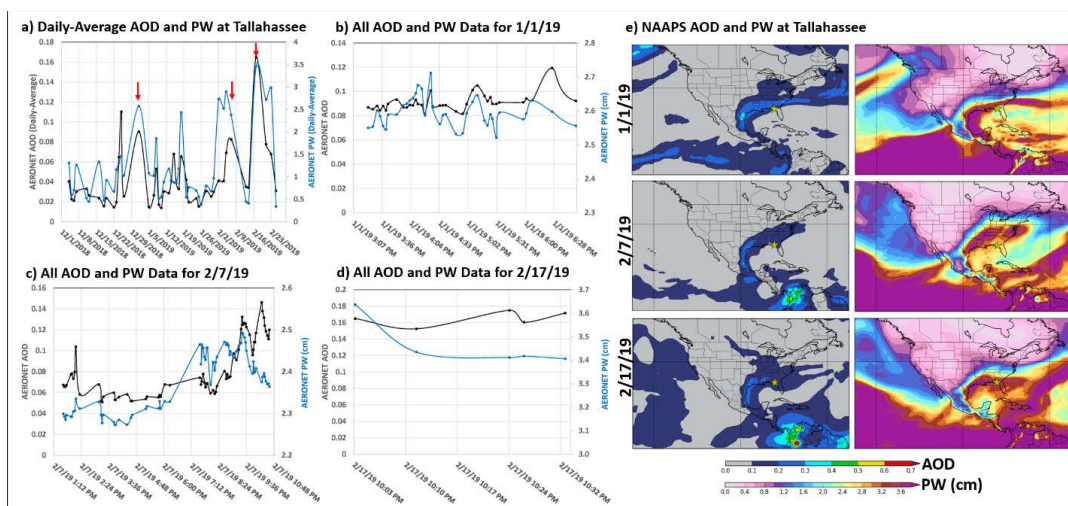
900   Figure 15. AOD and PW timeseries at the Tallahassee, Florida site in which strong positive correlations are observed during
901   the DJF season. The daily-average AOD and PW timeseries are shown for the 2018-2019 DJF season with red arrows
902   indicating select events for which joint peaks in AOD and PW are observed (a). Timeseries of AERONET data (non-
903   averaged, all data) for dates identified with red arrows are shown in timeseries b-d. Additionally, NAAPS-RA AOD and
904   PW (cm) fields are shown for the same dates with the AERONET site marked with a yellow star (e).

905
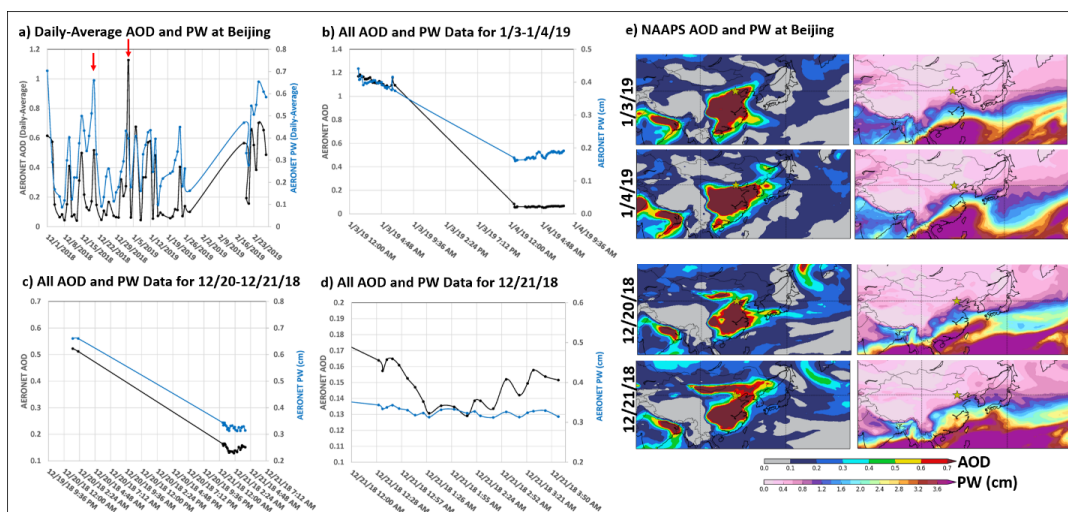
906   Figure 16. AOD and PW timeseries at the Beijing, China site in which strong positive correlations are observed during the
907   DJF season. The daily-average AOD and PW timeseries are shown for the 2018-2019 DJF season with red arrows indicating
908   select events for which joint peaks in AOD and PW are observed (a). Timeseries of AERONET data (non-averaged, all
909   data) for dates identified with red arrows are shown in timeseries b-d. Additionally, NAAPS-RA AOD and PW (cm) fields
910   are shown for the same dates with the AERONET site marked with a yellow star (e), including the air mass movement for
911   1/3-1/4/19 and 12/20-12/21/18.

912
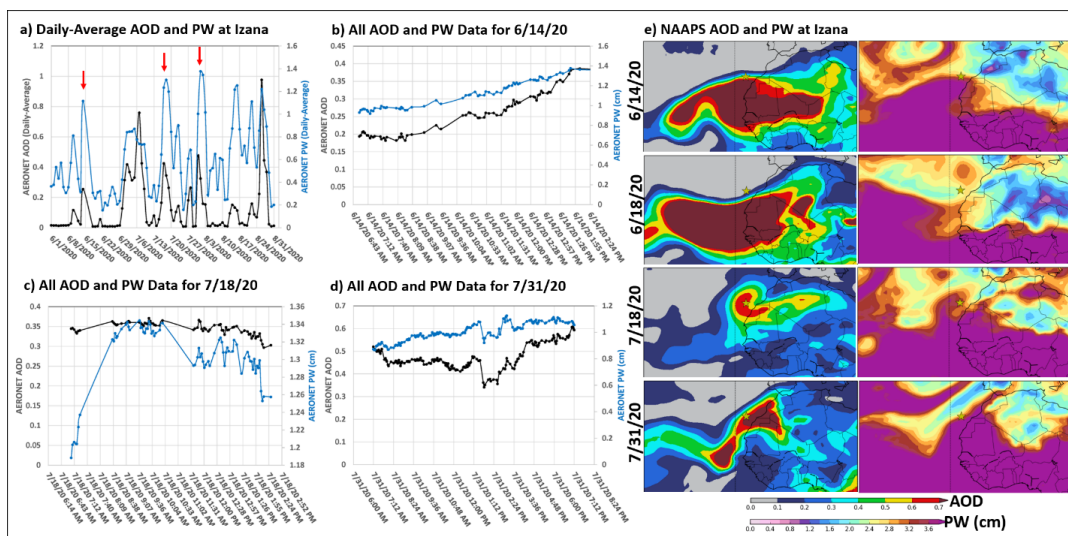
Figure 17. AOD and PW timeseries at the Izana, Canary Islands site in which strong positive correlations are observed during the JJA season. The daily-average AOD and PW timeseries are shown for the 2020 JJA season with red arrows indicating select events for which joint peaks in AOD and PW are observed (a). Timeseries of AERONET data (non-averaged, all data) for dates identified with red arrows are shown in timeseries b-d. Additionally, NAAPS-RA AOD and PW (cm) fields are shown for the same dates with the AERONET site marked with a yellow star (e). The fields for 6/18/20 are also included which show the joint dip in AOD and PW in the (a) timeseries after the 6/14 event.

919
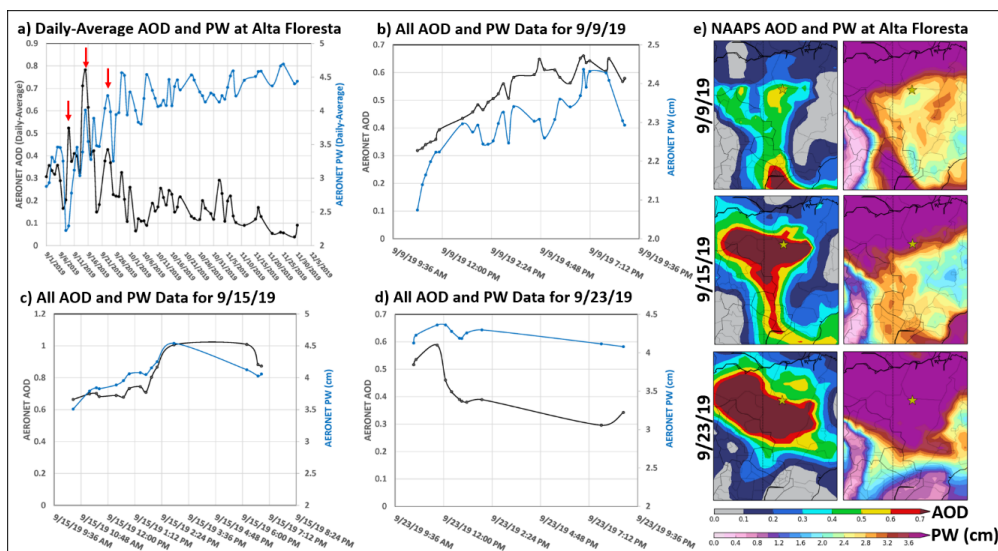
Figure 18. AOD and PW timeseries at the Alta Floresta site in Brazil in which negative AOD and PW correlations were identified in the seasonal analysis. The daily-average AOD and PW timeseries are shown for the 2019 SON season with red arrows indicating select events for further evaluation (a). AERONET AOD and PW timeseries (non-averaged, all data) for the selected events are shown in timeseries b-d. Additionally, NAAPS-RA AOD and PW (cm) fields are shown for the same dates with the AERONET site marked with a yellow star (e).

Atmospheric
Chemistry
and Physics
Discussions

926 **Table 1. AOD and PW relationship evaluation results for DJF at select AERONET sites that exhibited the strongest**
927 **AERONET correlations, positive and negative. The site name and latitude/longitude information are shown as well as the**
928 **correlation (R), change in AOD with PW (Slope), and the statistically significant difference in mean PW for high AOD**
929 **events (PW Diff) for both AERONET and the NAAPS-RA.**

AERONET Site	Lat	Lon	AERONET			NAAPS Reanalysis		
			R	Slope (cm^{-1})	PW Diff (cm)	R	Slope (cm^{-1})	PW Diff (cm)
Stennis	30.37	-89.62	0.743	0.044	1.082	0.739	0.042	1.156
Tallahassee	30.45	-84.30	0.739	0.024	1.068	0.664	0.037	0.901
Beijing-CAMS	39.93	116.32	0.707	1.016	0.225	0.755	1.132	0.347
XiangHe	39.75	116.96	0.673	1.349	0.196	0.755	1.132	0.347
SEARCH-Centreville	32.90	-87.25	0.665	0.028	0.931	0.706	0.045	1.000
Univ_of_Houston	29.72	-95.34	0.661	0.039	0.734	0.762	0.058	1.109
SEARCH-OLF	30.55	-87.38	0.659	0.025	0.820	0.720	0.039	1.069
Beijing	39.98	116.38	0.638	1.108	0.211	0.755	1.132	0.347
UAHuntsville	34.73	-86.64	0.633	0.029	0.930	0.684	0.049	0.866
UH_Coastal_Center	29.39	-95.04	0.624	0.039	0.862	0.762	0.058	1.109
Dhadnah	25.51	56.32	0.610	0.120	0.535	0.548	0.110	0.653
Ilorin	8.48	4.67	-0.261	-0.100	-0.513	-0.159	-0.063	-0.356
Pontianak	0.08	109.19	-0.345	-0.054	-0.476	-0.255	-0.029	-0.278
Koforidua_ANUC	6.11	-0.30	-0.459	-0.194	-0.894	-0.424	-0.178	-0.676
Jambi	-1.63	103.64	-0.473	-0.110	-0.942	-0.217	-0.039	-0.392
LAMTO-STATION	6.22	-5.03	-0.513	-0.214	-0.999	-0.331	-0.093	-0.644

930

931 **Table 2. AOD and PW relationship evaluation results for MAM at select AERONET sites that exhibited the strongest**
932 **AERONET correlations, positive and negative. The site name and latitude/longitude information are shown as well as the**
933 **correlation (R), change in AOD with PW (Slope), and the statistically significant difference in mean PW for high AOD**
934 **events (PW Diff) for both AERONET and the NAAPS-RA.**

AERONET Site	Lat	Lon	AERONET			NAAPS Reanalysis		
			R	Slope (cm^{-1})	PW Diff (cm)	R	Slope (cm^{-1})	PW Diff (cm)
UH_Coastal_Center	29.39	-95.04	0.694	0.041	1.099	0.665	0.068	1.058
UMBC	39.25	-76.71	0.680	0.042	1.219	0.602	0.053	0.870
Stennis	30.37	-89.62	0.680	0.046	0.967	0.630	0.048	0.978
NEON_OSBS	29.69	-81.99	0.679	0.032	1.241	0.511	0.038	0.737
NEON_TALL	32.95	-87.39	0.677	0.032	0.915	0.604	0.047	0.815
Univ_of_Houston	29.72	-95.34	0.666	0.048	1.000	0.665	0.068	1.058
UAHuntsville	34.73	-86.64	0.664	0.049	0.992	0.611	0.050	0.766
CCNY	40.82	-73.95	0.663	0.056	1.132	0.614	0.056	0.889
CASLEO	-31.80	-69.30	0.652	0.020	0.342	0.432	0.044	0.218
NEON_ORNL	35.96	-84.28	0.649	0.033	1.007	0.586	0.051	0.698
Nainital	29.36	79.46	0.629	0.256	0.422	0.388	0.112	0.457
Midway_Island	28.21	-177.38	-0.326	-0.033	-0.370	-0.323	-0.026	-0.490
Mandalay_MTU	21.97	96.19	-0.338	-0.049	-0.439	-0.384	-0.080	-0.717
LAMTO-STATION	6.22	-5.03	-0.353	-0.177	-0.429	-0.321	-0.132	-0.350
Vientiane	17.99	102.57	-0.355	-0.130	-0.451	-0.377	-0.144	-0.408
Chiang_Mai_Met_St	18.77	98.97	-0.372	-0.109	-0.586	-0.391	-0.126	-0.554
Jambi	-1.63	103.64	-0.392	-0.034	-1.265	-0.206	-0.020	-0.220
Ilorin	8.48	4.67	-0.392	-0.210	-0.710	-0.412	-0.151	-0.726
NGHIA_DO	21.05	105.80	-0.455	-0.216	-0.632	-0.318	-0.166	-0.349
Djougou	9.76	1.60	-0.500	-0.222	-0.836	-0.385	-0.114	-0.700

935

936

937

938 **Table 3. AOD and PW relationship evaluation results for JJA at select AERONET sites that exhibited the strongest**
939 **AERONET correlations, positive and negative. The site name and latitude/longitude information are shown as well as the**
940 **correlation (R), change in AOD with PW (Slope), and the statistically significant difference in mean PW for high AOD**
941 **events (PW Diff) for both AERONET and the NAAPS-RA. PW difference values of 0 in the NAAPS-RA indicate the change**
942 **was not statistically significant.**

AERONET Site	Lat	Lon	AERONET			NAAPS Reanalysis		
			R	Slope (cm^{-1})	PW Diff (cm)	R	Slope (cm^{-1})	PW Diff (cm)
Huambo	-12.87	15.70	0.737	0.365	0.447	0.467	0.174	0.350
DRAGON_OLNES	39.15	-77.07	0.731	0.088	0.894	0.399	0.048	0.386
Pretoria_CSIR-DPSS	-25.76	28.28	0.731	0.140	0.438	0.660	0.120	0.446
DRAGON_CLLGP	38.99	-76.91	0.719	0.085	1.097	0.348	0.039	0.387
Durban_UKZN	-29.82	30.94	0.711	0.111	0.670	0.687	0.131	0.567
Raciborz	50.08	18.19	0.672	0.065	0.749	0.614	0.085	0.578
Izana	28.31	-16.50	0.662	0.240	0.345	0.477	0.152	0.495
Helsinki	60.20	24.96	0.633	0.052	0.790	0.631	0.060	0.698
IMS-METU-ERDEML	36.57	34.26	0.632	0.099	0.543	0.559	0.073	0.484
CLUJ_UBB	46.77	23.55	0.632	0.091	0.529	0.602	0.100	0.438
Pokhara	28.19	83.98	-0.349	-0.111	-0.452	0.029	0.026	0.000
Bidi_Bahn	14.06	-2.45	-0.360	-0.175	-0.244	-0.251	-0.060	-0.305
Ouagadougou	12.42	-1.49	-0.385	-0.180	-0.292	-0.205	-0.059	-0.211
Lumbini	27.49	83.28	-0.388	-0.157	-0.434	-0.098	-0.013	-0.171
Dakar	14.39	-16.96	-0.418	-0.146	-0.528	-0.428	-0.122	-0.584
Agoufou	15.35	-1.48	-0.491	-0.209	-0.533	-0.258	-0.060	-0.346
IER_Cinzana	13.28	-5.93	-0.501	-0.269	-0.424	-0.279	-0.077	-0.259
Jomsom	28.78	83.71	-0.646	-0.064	-0.581	0.029	0.026	0.000

943

944 **Table 4. AOD and PW relationship evaluation results for SON at select AERONET sites that exhibited the strongest**
945 **AERONET correlations, positive and negative. The site name and latitude/longitude information are shown as well as the**
946 **correlation (R), change in AOD with PW (Slope), and the statistically significant difference in mean PW for high AOD**
947 **events (PW Diff) for both AERONET and the NAAPS-RA. PW difference values of 0 in the NAAPS-RA indicate the change**
948 **was not statistically significant.**

AERONET Site	Lat	Lon	AERONET			NAAPS Reanalysis		
			R	Slope (cm^{-1})	PW Diff (cm)	R	Slope (cm^{-1})	PW Diff (cm)
USDA	39.03	-76.88	0.815	0.088	1.883	0.570	0.036	1.043
SEARCH-Centreville	32.90	-87.25	0.796	0.026	1.748	0.531	0.032	0.917
St_Louis_University	38.64	-90.23	0.724	0.032	1.369	0.574	0.037	1.188
Martova	49.94	36.95	0.706	0.070	0.590	0.531	0.064	0.633
UMBC	39.25	-76.71	0.699	0.035	1.473	0.570	0.036	1.043
Poprad-Ganovce	49.04	20.32	0.689	0.053	0.651	0.568	0.071	0.525
NEON_TALL	32.95	-87.39	0.679	0.025	1.184	0.531	0.032	0.917
GISS	40.80	-73.96	0.673	0.062	1.369	0.556	0.033	0.950
Harvard_Forest	42.53	-72.19	0.666	0.035	1.051	0.576	0.036	1.020
Mingo	36.97	-90.14	0.655	0.040	1.500	0.594	0.038	1.186
Dhadnah	25.51	56.32	0.651	0.106	0.757	0.643	0.115	0.706
Midway_Island	28.21	-177.38	-0.344	-0.013	-0.431	-0.172	-0.007	-0.339
Alta_Floresta	-9.87	-56.10	-0.382	-0.148	-0.573	-0.470	-0.197	-0.634
Koforidua_ANUC	6.11	-0.30	-0.384	-0.161	-0.173	-0.252	-0.046	-0.330
Rio_Branco	-9.96	-67.87	-0.426	-0.121	-0.496	-0.430	-0.145	-0.643
Abracos_Hill	-10.76	-62.36	-0.430	-0.226	-0.351	-0.401	-0.205	-0.373
Ilorin	8.48	4.67	-0.431	-0.091	-0.653	-0.227	-0.033	-0.476
Palangkaraya	-2.23	113.95	-0.443	-0.385	-0.549	-0.512	-0.195	-0.886
Ji_Parana_SE	-10.93	-61.85	-0.483	-0.197	-0.659	-0.412	-0.203	-0.393
Pontianak	0.08	109.19	-0.536	-0.521	-0.644	-0.400	-0.145	-0.454
Kuching	1.49	110.35	-0.552	-0.373	-0.528	-0.329	-0.111	-0.360

949

Atmospheric
Chemistry
and Physics
Discussions

950   **References**

951   American Meteorological Society, 2020: Aerosol. Glossary of
952   Meteorology, http://glossary.ametsoc.org/wiki/climatology. Last accessed Jan 2021.

953   Adebiyi, A. A., Zuidema, P., and Abel, S. J.: The Convolution of Dynamics and Moisture with the Presence of
954   Shortwave Absorbing Aerosols over the Southeast Atlantic, Journal of Climate, 28, 1997–2024,
955   https://doi.org/10.1175/JCLI-D-14-00352.1, 2015.

956   Arola, A., Eck, T. F., Kokkola, H., Pitkänen, M. R. A., and Romakkaniemi, S.: Assessment of cloud-related fine-
957   mode AOD enhancements based on AERONET SDA product, Atmos. Chem. Phys., 17, 5991–6001,
958   https://doi.org/10.5194/acp-17-5991-2017, 2017.

959   Barreto, Á., Cuevas, E., García, R. D., Carrillo, J., Prospero, J. M., Ilić, L., Basart, S., Berjón, A. J., Marrero, C. L.,
960   Hernández, Y., Bustos, J. J., Ničković, S., and Yela, M.: Long-term characterization of the vertical structure of the
961   Saharan Air Layer over the Canary Islands using lidar and radiosonde profiles: implications for radiative and cloud
962   processes over the subtropical Atlantic Ocean, Atmos. Chem. Phys., 22, 739–763, https://doi.org/10.5194/acp-22-
963   739-2022, 2022.

964   Benedetti, A., Morcrette, J.-J., Boucher, O., Dethof, A., Engelen, R. J., Fisher, M., Flentje, H., Huneeus, N., Jones,
965   L., Kaiser, J. W., Kinne, S., Mangold, A., Razinger, M., Simmons, A. J., and Suttie, M.: Aerosol analysis and recast
966   in the European centre for Medium-Range Weather Forecasts Integrated Forecast
967   System: 2. Data assimilation, J. Geophys. Res., 114, D13205, doi:10.1029/2008JD011115, 2009.

968   Charlson, R.J., S.E. Schwartz, J.M. Hales, R.D. Cess, J.A. Coakley, Jr., J.E. Hansen, and D.J. Hoffman: Climate
969   forcing by anthropogenic aerosols. *Science*, 255, 423-430, doi:10.1126/science.255.5043.423, 1992.

970   Daley, R. and Barker, E.: NAVDAS: Formulation and diagnostics, Mon. Weather Rev., 129, 869–883,
971   https://doi.org/10.1175/1520-0493(2001)129, 2001.

972   Deaconu, L. T., Ferlay, N., Waquet, F., Peers, F., Thieuleux, F., and Goloub, P.: Satellite inference of water vapour
973   and above-cloud aerosol combined effect on radiative budget and cloud-top processes in the southeastern Atlantic
974   Ocean, Atmos. Chem. Phys., 19, 11613–11634, https://doi.org/10.5194/acp-19-11613-2019, 2019.

975   DeSouza-Machado, S. G., Strow, L. L., Hannon, S. E., and Motteler, H. E.: Infrared dust spectral signatures from
976   AIRS, Geophys. Res. Lett., 33, L03801, doi:10.1029/2005GL024364, 2006.

977   De Tomasi, F., and Perrone, M. R.: Lidar measurements of tropospheric water vapor and aerosol profiles over
978   southeastern Italy, J. Geophys. Res., 108, 4286, doi:10.1029/2002JD002781, 2003.

979   Eck, T. F., and Holben, B. N.: AVHRR split window temperature differences and total precipitable water over land
980   surfaces, International Journal of Remote Sensing, 15:3, 567-582, doi: 10.1080/01431169408954097, 1994.

981   Eck, T. F., Holben B. N., Reid, J. S., Dubovik, O., Smirnov, A., O'Neill, N. T., Slutsker, I., and Kinne, S.:
982   Wavelength dependence of the optical depth of biomass burning, urban, and desert
983   dust aerosols, J. Geophys. Res., 104, 31333–31349, DOI: 10.1029/1999JD900923, 1999.

984   Eck, T.F., Holben, B.N., Reid, J.S., Giles, D.M., Rivas, M.A., Singh, R.P., Tripathi, S.N., Bruegge, C.J., Platnick,
985   S., Arnold, G.T., Krotkov, N.A., Carn, S.A., Sinyuk, A., Dubovik, O., Arola, A., Schafer, J.S., Artaxo, P., Smirnov,
986   A., Chen, H., Goloub, P.: Fog- and cloud-induced aerosol modification observed by the Aerosol Robotic Network
987   (AERONET), J. Geophys. Res., 117, D07206,doi:10.1029/2011JD016839, 2012.

988   Eck, T. F., Holben, B. N., Reid, J. S., Arola, A., Ferrare, R. A., Hostetler, C. A., Crumeyrolle, S. N., Berkoff, T. A.,
989   Welton, E. J., Lolli, S., Lyapustin, A., Wang, Y., Schafer, J. S., Giles, D. M., Anderson, B. E., Thornhill, K. L.,
990   Minnis, P., Pickering, K. E., Loughner, C. P., Smirnov, A., and Sinyuk, A.: Observations of rapid aerosol optical
991   depth enhancements in the vicinity of polluted cumulus clouds, Atmos. Chem. Phys., 14, 11633–11656,
992   https://doi.org/10.5194/acp-14-11633-2014, 2014.

993   Eck, T. F., Holben, B. N., Reid, J. S., Xian, P.,Giles, D. M., Sinyuk, A., Smirnov, A., Schafer, J.S., Slutsker, I., Kim,
994   J., Koo, J.-H., Choi, M., Kim, K.C., Sano, I., Arola, A., Sayer, A.M., Levy, R.C., Munchak, L.A., O'Neill, N.T.,
995   Lyapustin, A., Hsu, N.C., Randles, C.A., Da Silva, A.M., Buchard, V., Govindaraju, R.C., Hyer, E., Crawford, J.H.,
996   Wang, P., Xia, X.: Observations of the interaction and transport offine mode aerosols with cloud and/or fog in

997   Northeast Asia from Aerosol Robotic Network and satellite remote sensing.Journal of GeophysicalResearch:
998   Atmospheres,123, 5560–5587.https://doi.org/10.1029/2018JD028313, 2018.

999   Eck, T.F., Holben, B.N., Giles, D.M., Slutsker, I., Sinyuk, A., Schafer, J.S., Smirnov, A., Sorokin, M., Reid, J.S.,
1000   Sayer, A.M., Hsu, N.C., Shi, Y.R., Levy, R.C., Lyapustin, A., Rahman, M.A., Liew, S.-C., Cortijo, S.V.S., Li, R.,
1001   Kalbermatter, D., Keong, K.L., Yuggotomo, M.E., Aditya, F., Mohamad, M., Mahmud, M., Chong, T.K., Lim, H.-
1002   S., Choon, Y.E., Deranadyan, G., Kusumaningtyas, S.D.A., Aldrian, E.: AERONET Remotely Sensed
1003   Measurements and Retrievals of Biomass Burning Aerosol Optical Properties During the 2015 Indonesian Burning
1004   Season, J. Geophys. Res., 124, 4722–4740.https://doi.org/10.1029/2018JD030182, 2019.

1005   Francis, D., Fonseca, R., Nelli, N., Cuesta, J., Weston, M., Evan, A., and Temimi, M: The atmospheric drivers of the
1006   major Saharan dust storm in June 2020, Geophys. Res. Lett., 47, e2020GL090102.
1007   https://doi.org/10.1029/2020GL090102, 2020.

1008   Frouin, R.J., Franz, B.A., Ibrahim, A., Knobelspiesse, K., Ahmad, Z., Cairns, B., Chowdhary, J., Dierssen, H.M.,
1009   Tan, J., Dubovik, O., Huang, X., Davis, A.B. , Kalashnikova, O., Thompson, D.R., Remer, L.A., Boss, E.,
1010   Coddington, O., Deschamps, P.-Y., Gao, B.-C., Gross, L., Hasekamp, O., Omar, A., Pelletier, B., Ramon, D.,
1011   Steinmetz, F., and Zhai, P.-W.: Atmospheric correction of satellite ocean-color imagery during the PACE Era. Front.
1012   Earth Sci., 7, 145, doi:10.3389/feart.2019.00145, 2019.

1013   Gao, M., Carmichael, G. R., Saide, P. E., Lu, Z., Yu, M., Streets, D. G., and Wang, Z.: Response of winter fine
1014   particulate matter concentrations to emission and meteorology changes in North China, Atmos. Chem. Phys., 16,
1015   11837–11851, https://doi.org/10.5194/acp-16-11837-2016, 2016.

1016   Giles, D. M., Sinyuk, A., Sorokin, M. G., Schafer, J. S., Smirnov, A., Slutsker, I., Eck, T. F., Holben, B. N., Lewis,
1017   J. R., Campbell, J. R., Welton, E. J., Korkin, S. V., and Lyapustin, A. I.: Advancements in the Aerosol Robotic
1018   Network (AERONET) Version 3 database – automated near-real-time quality control algorithm with improved
1019   cloud screening for Sun photometer aerosol optical depth (AOD) measurements, Atmos. Meas. Tech., 12, 169–209,
1020   https://doi.org/10.5194/amt-12-169-2019, 2019.

1021   Gobbi, G.P., Barnaba, F., Di Liberto, L., Bolignano, A., Lucarelli, F., Nava, S., Perrino, C., Pietrodangelo, A.,
1022   Basart, S., Costabile, F., Dionisi, D., Rizza, U., Canepari, S., Sozzi, R., Morelli, M., Manigrasso, M., Drewnick, F.,
1023   Struckmeier, C., Poenitz, K., Wille, H.: An inclusive view of Saharan dust advections to Italy and the Central
1024   Mediterranean, Atmospheric Environment, Volume 201, 2019, Pages 242-256,ISSN 1352-2310,
1025   https://doi.org/10.1016/j.atmosenv.2019.01.002, 2019.

1026   Granados-Muñoz, M. J., Sicard, M., Román, R., Benavent-Oltra, J. A., Barragán, R., Brogniez, G., Denjean, C.,
1027   Mallet, M., Formenti, P., Torres, B., and Alados-Arboledas, L.: Impact of mineral dust on shortwave and longwave
1028   radiation: evaluation of different vertically resolved parameterizations in 1-D radiative transfer computations ,
1029   Atmos. Chem. Phys., 19, 523–542, https://doi.org/10.5194/acp-19-523-2019, 2019.

1030   Gutleben, M., Groß, S., Wirth, M., Emde, C., & Mayer, B.: Impacts of water vapor on Saharan air layer radiative
1031   heating. Geophysical Research Letters, 46, 14854– 14862, https://doi.org/10.1029/2019GL085344, 2019.

1032   Haywood, J. M., Bellouin, N., Jones, A., Boucher, O., Wild, M., and Shine, K. P.: The roles of aerosol, water vapor
1033   and cloud in future global dimming/brightening, J. Geophys. Res., 116, D20203, doi:10.1029/2011JD016000, 2011.

1034   Hänel, G.: The properties of atmospheric aerosol particles as functions of the relative humidity at thermo- dynamic
1035   equilibrium with the surrounding moist air. Adv. Geophys. 19, 73-18, https://doi.org/10.1016/S0065-
1036   2687(08)60142-9, 1976.

1037   He Q., Ma, J., Zheng, X., Wang, Y., Wang Y., Mu, H., Cheng, T., He, R., Huang, G., Liu, D.: Formation and
1038   dissipation dynamics of the Asian tropopause aerosol layer, Environ. Res. Lett, 16, 014015,
1039   https://doi.org/10.1088/1748-9326/abcd5d, 2021.

1040   Heo, J.-H.; Ryu, G.-H.; Jang, J.-D. Optimal Interpolation of Precipitable Water Using Low Earth Orbit and
1041   Numerical Weather Prediction Data. Remote Sens. 2018, 10, 436.

1042   Hogan, T. F., Liu, M., Ridout, J. S., Peng, M. S., Whitcomb, T. R., Ruston, B. C., Reynolds, C. A., Eckermann S.
1043   D., Moskaitis, J. R., Baker, N. L., McCormack, J. P., Viner, K. C., McLay, J. G., Flatau, M. K., Xu, L., Chen, C.,
1044   and Chang, S. W.: The Navy Global Environmental Model. Oceanography, Special Issue on Navy Operational
1045   Models, 27, No. 3. 2014.

Holben, B. N., Eck, T. F., Slutsker, I., Tanré, D., Buis, J. P., Setzer, A., Vermote, E., Reagan, J. A., Kaufman, Y. J., Nakajima, T., Lavenu, F., Jankowiak, I., & Smirnov, A.: AERONET - A federated instrument network and data archive for aerosol characterization. Remote Sensing of Environment, 66(1), 1-16, https://doi.org/10.1016/S0034-4257(98)00031-5, 1998.

Huttunen, J., Arola, A., Myhre, G., Lindfors, A. V., Mielonen, T., Mikkonen, S., Schafer, J. S., Tripathi, S. N., Wild, M., Komppula, M., and Lehtinen, K. E. J.: Effect of water vapor on the determination of aerosol direct radiative effect based on the AERONET fluxes, Atmos. Chem. Phys., 14, 6103–6110, https://doi.org/10.5194/acp-14-6103-2014, 2014.

Ibrahim, A., Franz, B.A., Ahmad, Z., and Bailey, S.W.: Multiband atmospheric correction algorithm for ocean color retrievals, Front. Earth Sci., https://doi.org/10.3389/feart.2019.00116, 2019.

Ichoku, C., Allen Chu, D., Mattoo, S., Kaufman, Y.J., Remer, L.A., Tanre, D., Slutsker, I., and Holben, B.N.: A spatio-temporal approach for global validation and analysis of MODIS aerosol products, Geophysical Research Letters, 29(12), https://doi.org/10.1029/2001GL013206, 2002.

Jeong, J.I., and Park, R.J.: Winter monsoon variability and its impact on aerosol concentrations in East Asia, Environmental Pollution, Volume 221, Pages 285-292, https://doi.org/10.1016/j.envpol.2016.11.075, 2017.

Jung, E., Albrecht, B., Prospero, J. M., Jonsson, H. H., & Kreidenweis, S. M.: Vertical structure of aerosols, temperature, and moisture associated with an intense African dust event observed over the eastern Caribbean. Journal of Geophysical Research Atmospheres, 118, 4623– 4643. https://doi.org/10.1002/jgrd.50352, 2013.

Kahn, R.A., Gaitley, B.J., Martonchik, J.V., Diner, D.J., Crean, K.A. and Holben, B.: Multiangle Imaging Spectroradiometer (MISR) global aerosol optical depth validation based on 2 years of coincident Aerosol Robotic Network (AERONET) observations. Journal of Geophysical Research 110: doi: 10.1029/2004JD004706. issn: 0148-0227, 2005.

Kanitz, T., Ansmann, A., Seifert, P., Engelmann, R., Kalisch, J., & Althausen, D.: Radiative effect of aerosols above the northern and southern Atlantic Ocean as determined from shipborne lidar observations. Journal of Geophysical Research; Atmospheres, 118, 12,556– 12,565. https://doi.org/10.1002/2013jd019750, 2013.

Kanitz, T., Engelmann, R., Heinold, B., Baars, H., Skupin, A., & Ansmann, A.: Tracking the Saharan air layer with shipborne lidar across the tropical atlantic. Geophysical Research Letters, 41, 1044– 1050. https://doi.org/10.1002/2013gl058780, 2014.

Kannemadugu, H.B.S., Varghese, A.O., Mukkara, S.R., Joshi, A.K. and Moharil, S.V.: Discrimination of Aerosol Types and Validation of MODIS Aerosol and Water Vapour Products Using a Sun Photometer over Central India. Aerosol Air Qual. Res. 15: 682-693. https://doi.org/10.4209/aaqr.2014.04.0088, 2015.

Karyampudi, V. M., Palm, S.P., Reagen, J.A., Fang, H., Grant, W.B, Hoff, R.M., Moulin, C., Pierce, H.F., Torres, O., Browell, E.V., and Melfi, S.H.: Validation of the Saharan dust plume conceptual model using Lidar, Meteosat, and ECMWF data, Bull. Am. Meteorol. Soc., 80, 1045 – 1074, https://doi.org/10.1175/1520-0477(1999), 1999.

Kaufman, Y. J., and Fraser, R. S.: The effect of smoke particles on clouds and climate forcing, Science, 277, 1636-1639, DOI: 10.1126/science.277.5332.1636, 1997.

Kim, S.-W., Chazette, P., Dulac, F., Sanak, J., Johnson, B., and Yoon, S.-C.: Vertical structure of aerosols and water vapor over West Africa during the African monsoon dry season, Atmos. Chem. Phys., 9, 8017–8038, https://doi.org/10.5194/acp-9-8017-2009, 2009.

Kleinman, L.I., and Daum, P.H.: Vertical distribution of aerosol particles, water vapor, and insoluble trace gases in convectively mixed air, J. Geophys. Res. Atmos.,96 (D1), 991-1005, https://doi.org/10.1029/90JD02117, 1991.

Kuciauskas, A. P., Xian, P., Hyer, E. J., Oyola, M. I., & Campbell, J. R.: Supporting Weather Forecasters in Predicting and Monitoring Saharan Air Layer Dust Events as They Impact the Greater Caribbean, Bulletin of the American Meteorological Society, 99(2), 259-268, https://doi.org/10.1175/BAMS-D-16-0212.1, 2018.

Kumar, K. R., Sivakumar, V., Reddy, R. R., Gopal, K. R., Adesina, A. J.: Inferring wavelength dependence of AOD and Ångström exponent over a sub-tropical station in South Africa using AERONET data: Influence of

1093 meteorology, long-range transport and curvature effect, Science of The Total Environment, 461, 397-408,
1094 https://doi.org/10.1016/j.scitotenv.2013.04.095, 2013.

1095 Kumar, K. R., Kang, N., Sivakumar, V., Griffith, D.: Temporal characteristics of columnar aerosol optical properties
1096 and radiative forcing (2011–2015) measured at AERONET's Pretoria_CSIR_DPSS site in South Africa,
1097 Atmospheric Environment,165, 274-289, https://doi.org/10.1016/j.atmosenv.2017.06.048., 2017.

1098 Lee, E., Županski, M., Županski, D. and Park, S. K.: Impact of the OMI aerosol optical depth on analysis increments
1099 through coupled meteorology–aerosol data assimilation for an Asian dust storm, Remote Sens. Environ., 193, 38–
1100 53, 30 doi:10.1016/j.rse.2017.02.013, 2017.

1101 Li, Q., Zhang, R., and Wang, Y.: Interannual variation of the wintertime fog-haze days across central and eastern
1102 China and its relation with East Asian winter monsoon, International Journal of Climatology, 36(1),
1103 https://doi.org/10.1002/joc.4350, 2016.

1104 Li, J., Liao, H., Hu, J., Li, N., Severe particulate pollution days in China during 2013-2018 and the associated typical
1105 weather patterns in Beijing-Tianjin-Hebei and the Yangtze River Delta regions. Environmental Pollution, 248, 74-
1106 81, https://doi.org/10.1016/j.envpol.2019.01.124, 2019.

1107 Liu, Z., Liu, Q., Lin, H. C., Schwartz, C. S., Lee, Y. H. and Wang, T.: Three-dimensional variational assimilation of
1108 MODIS aerosol optical depth: Implementation and application to a dust storm over East Asia, J. Geophys. Res.
1109 Atmos., 116(23), 1– 19, doi:10.1029/2011JD016159, 2011.

1110 Liu, D., Zhao, T., Boiyo, R., Chen, S., Lu, Z., Wu, Y., Zhao, Y.: Vertical structures of dust aerosols over East Asia
1111 based on CALIPSO retrievals. Remote Sens., 11,701; doi:10.3390/rs11060701, 2019.

1112 Livingston, J. M., Russell, P. B., Reid, J. S., Redemann, J., Schmidt, B., Allen, D. A., Torres, O., Levy, R. C.,
1113 Remer, L. A., Holben, B. N.m Smirnov, A., Dubovik, O., Welton, E. J., Campbell, J. R., Wang, J., Christopher, S.
1114 A.: Airborne Sun photometer measurements of aerosol optical depth and columnar water vapor during the Puerto
1115 Rico Dust Experiment and comparison with land, aircraft, and satellite measurements, J. Geophys. Res., 108, 8588,
1116 doi:10.1029/2002JD002520, D19, 2003.

1117 Luo, B., Minnett, P.J., Gentemann, C., and Szczodrak, G.: Improving satellite retrieved night-time infrared sea
1118 surface temperatures in aerosol contaminated regions. Remote Sensing of Environment, 223,8-20,
1119 https://doi.org/10.1016/j.rse.2019.01.009, 2019.

1120 Lynch, P., Reid, J. S., Westphal, D. L., Zhang, J., Hogan, T. F., Hyer, E. J., Curtis, C. A., Hegg, D. A., Shi, Y.,
1121 Campbell, J. R., Rubin, J. I., Sessions, W. R., Turk, F. J., and Walker, A. L.: An 11-year global gridded aerosol
1122 optical thickness reanalysis (v1.0) for atmospheric and climate sciences, Geosci. Model Dev., 9, 1489–1522,
1123 https://doi.org/10.5194/gmd-9-1489-2016, 2016.

1124 Marsham, J. H., Parker, D. J., Grams, C. M., Johnson, B. T., Grey, W. M. F., & Ross, A. N.: Observations of
1125 mesoscale and boundary-layer scale circulations affecting dust transport and uplift over the Sahara. Atmospheric
1126 Chemistry and Physics, 8(23), 6979– 6993, https://doi.org/10.5194/acp-8-6979-2008, 2008.

1127 Marsham, J. H., Parker, D. J., Todd, M. C., Banks, J. R., Brindley, H. E., Garcia-Carreras, L., Roberts, A. J., and
1128 Ryder, C. L.: The contrasting roles of water and dust in controlling daily variations in radiative heating of the
1129 summertime Saharan heat low, Atmos. Chem. Phys., 16, 3563–3575, https://doi.org/10.5194/acp-16-3563-2016,
1130 2016.

1131 Martins, V. S., Novo, E. M. L. M., Lyapustin, A., Aragão, L. E. O. C., Freitas, S. R., Barbosa, C. C. F: Seasonal and
1132 interannual assessment of cloud cover and atmospheric constituents across the Amazon (2000–2015): Insights for
1133 remote sensing and climate analysis, ISPRS Journal of Photogrammetry and Remote Sensing,145, 309-327,
1134 https://doi.org/10.1016/j.isprsjprs.2018.05.013, 2018.

1135 Ménard, R., Gauthier, P., Rochon, Y., Robichaud, A., de Grandpré, J., Yang, Y., Charrette, C., and Chabrillat, S.:
1136 Coupled Stratospheric Chemistry–Meteorology Data Assimilation. Part II: Weak and Strong
1137 Coupling. Atmosphere, 10, 798, https://doi.org/10.3390/atmos10120798 , 2019.

1138 Mortier, A., Goloub, P., Derimian, Y., Tanre, D., Podvin, T., Blarel, L., Deroo, C., Marticorena, B., Diallo, A., and
1139 Ndiaye, T.: Climatology of aerosol properties and clear-sky shortwave radiative effects using Lidar and Sun
1140 photometer observations in the Dakar site, J. Geophys. Res. Atmos., 121(11),
1141 https://doi.org/10.1002/2015JD024588, 2016.

O'Neill, N. T., Royer, A., Coté, P., McArthur, L. J. B., Relations between optically derived aerosol parameters, humidity, and air-quality data in an urban atmosphere, J. Appl Meteor., 32, 1484-1498, https://doi.org/10.1175/1520-0450(1993)032<1484:RBODAP>2.0.CO;21993, 1993.

Patadia, F., Levy, R. C., and Mattoo, S.: Correcting for trace gas absorption when retrieving aerosol optical depth from satellite observations of reflected shortwave radiation, Atmos. Meas. Tech., 11, 3205–3219, https://doi.org/10.5194/amt-11-3205-2018, 2018.

Perez-Ramirez, D., Whiteman, D.N., Smirnov, A., Lyamani, H., Holben, B.N., Pinker, R., Andrade, M., Alados-Arboledas, L.: Evaluation of AERONET precipitable water vapor versus microwave radiometry, GPS, and radiosondes at ARM sites, J. Geophys. Res. Atmos, 119(15), https://doi.org/10.1002/2014JD021730, 2014.

Perry, K.D., and Hobbs P.V.: Influences of isolated cumulus clouds on the humidity of their surroundings Journal of the Atmospheric Sciences. 53: 159-174. DOI: https://doi.org/10.1175/1520-0469(1996)053<0159:IOICCO>2.0.CO;2, 1996.

Pistone, K., Praveen, P. S., Thomas, R. M., Ramanathan, V., Wilcox, E. M., and Bender, F. A.-M.: Observed correlations between aerosol and cloud properties in an Indian Ocean trade cumulus regime, Atmos. Chem. Phys., 16, 5203–5227, https://doi.org/10.5194/acp-16-5203-2016, 2016.

Pistone, K., Zuidema, P., Wood, R., Diamond, M., da Silva, A. M., Ferrada, G., Saide, P. E., Ueyama, R., Ryoo, J.-M., Pfister, L., Podolske, J., Noone, D., Bennett, R., Stith, E., Carmichael, G., Redemann, J., Flynn, C., LeBlanc, S., Segal-Rozenhaimer, M., and Shinozuka, Y.: Exploring the elevated water vapor signal associated with the free tropospheric biomass burning plume over the southeast Atlantic Ocean, Atmos. Chem. Phys., 21, 9643–9668, https://doi.org/10.5194/acp-21-9643-2021, 2021.

Radke L.F., and Hobbs, P.V.: Humidity and particle fields around some small cumulus clouds, Journal of the Atmospheric Sciences. 48: 1190-1193. DOI: 10.1175/1520-0469(1991), 1991.

Reid, J. S., Kinney, J. E., Westphal, D. L., Holben, B. N., Welton, E. J., Tsay, S.-C., Christopher, S. A., Eleuterio, D. P., Campbell, J. R., Jonsson, H. H., Livingston, J. M., Maring, H. B., Meier, M., Pilewskie, P., Reid, E. A., . Russell, P. B., Savoie, D., Smironov, A., and D. Tanré D.: Analysis of measurements of Saharan dust by airborne and ground-based remote sensing methods during the Puerto Rico Dust Experiment (PRIDE), J. Geophys. Res., 108, 8586, doi:10.1029/2002JD002493, D19, 2003.

Reid, J. S., Piketh, S., Burger, R., Ross, K., Jensen, T., Bruintjes, R., Walker, A., Al Mandoos, A., Miller, S., Hsu, C., Kuciauskas, A., and Westphal. , D. L.: An overview of UAE2 flight operations: Observations of summertime atmospheric thermodynamic and aerosol profiles of the southern Arabian Gulf, J. Geophys. Res., 113, D14213, doi:10.1029/2007JD009435, 2008.

Reid, J. S., Hyer, E. J., Johnson, R., Holben, B. N., Yokelson, R. J., Zhang, J., Campbell, J.R., Christopher, S.A., Di Girolamo, L., Giglio, L., Holz, R.E., Kearney, C., Miettinen, J., Reid, E.A., Turk, F.J., Wang, J., Xian, P., Zhao, G., Balasubramanian, R., Chew, B.N., Janjai, S., Lagrosas, N., Lestari, P., Lin, N.-H., Mahmud, M., Nguyen, A.X., Norris, B., Oanh, N.T.K., Oo, M., Salinas, S.V., Welton, E.J., and Liew, S.C.: Observing and understanding the Southeast Asian aerosol system by remote sensing: An initial review and analysis for the Seven Southeast Asian Studies (7SEAS) program. Atmospheric Research, 122, 403–468. https://doi.org/10.1016/j.atmosres.2012.06.005, 2013.

Reid, J. S., Posselt, D. J., Kaku, K., Holz, R. A., Chen, G., Eloranta, E. W., Kuehn, R. E., Woods, S., Zhang, J., Anderson, B., Bui, T. P., Diskin, G. S., Minnis, P., Newchurch, M. J., Tanelli, S., Trepte, C. R., Thornhill, K. L., and Ziemba, L. D.: Observations and hypotheses related to low to middle free tropospheric aerosol, water vapor and altocumulus cloud layers within convective weather regimes: a SEAC4RS case study, Atmos. Chem. Phys., 19, 11413–11442, https://doi.org/10.5194/acp-19-11413-2019, 2019.

Reid, J.S., Gumber, A., Zhang, J., Holz, R.E., Rubin, J.I., Xian, P., Smirnov, A., Eck, T.F., O'Neill, N.T., Levy R.C., Reid, E.A., Colarco, P.R., Benedetti, A., Tanaka, T.: A Coupled Evaluation of Operational MODIS and Model Aerosol Products for Maritime Environments Using Sun Photometry: Evaluation of the Fine and Coarse Mode. Remote Sensing; 14(13):2978. https://doi.org/10.3390/rs14132978, 2022.

Remer, L.A., Tanre, D., Kaufman, Y.J., Ichoku, C., Mattoo, S., Levy, R., Chu, D.A., Holben, B., Dubovik, O., Smirnov, A., Martins, J.V., Li, R.-R, and Ahmad, Z.: Validation of MODIS aerosol retrieval over ocean, Geophysical Research Letters, 29(12), 1618, https://doi.org/10.1029/2001GL013204, 2002.

Resquin, M.D., Santagata, D., Gallardo, L., Gomez, D., Rossler, C., Dawidowski, L.: Local and remote black carbon sources in the Metropolitan Area of Buenos Aires. Atmospheric Environment. Volume 182, Pages 105-114, https://doi.org/10.1016/j.atmosenv.2018.03.018, 2018.

Rosário, N. E., Yamasoe, M. A., Brindley, H., Eck, T. F., and Schafer, J.: Downwelling solar irradiance in the biomass burning region of the southern Amazon: Dependence on aerosol intensive optical properties and role of water vapor, J. Geophys. Res., 116, D18304, doi:10.1029/2011JD015956, 2011.

Ryder, C. L.: Radiative effects of increased water vapor in the upper Saharan Air Layer associated with enhanced dustiness. Journal of Geophysical Research: Atmospheres, 126, e2021JD034696, https://doi.org/10.1029/2021JD034696, 2021.

Sano, I., Mukai, S., Yamauo, M., Takamura, T., Nakajima, T., and Holben, B.: Calibration and Validation of Retrieved Aerosol Properties Based on AERONET and SKYNET, Advances in Space Research 32 (11): 2159–2164. doi:10.1016/S0273-1177(03)00685-9, 2003.

Schneider, T., O'Gorman, P.A., and Levine, X.J.: Water vapor and the dynamics of climate changes, Rev. Geophys., 48, RG3001, doi:10.1029/2009RG000302, 2010.

Sessions, W. R., Reid, J. S., Benedetti, A., Colarco, P. R., da Silva, A., Lu, S., Sekiyama, T., Tanaka, T. Y., Baldasano, J. M., Basart, S., Brooks, M. E., Eck, T. F., Iredell, M., Hansen, J. A., Jorba, O. C., Juang, H.-M. H., Lynch, P., Morcrette, J.-J., Moorthi, S., Mulcahy, J., Pradhan, Y., Razinger, M., Sampson, C. B., Wang, J., and Westphal, D. L.: Development towards a global operational aerosol consensus: basic climatological characteristics of the International Cooperative for Aerosol Prediction Multi-Model Ensemble (ICAP-MME), Atmos. Chem. Phys., 15, 335–362, doi:10.5194/acp-15-335-2015, 2015.

Sherwood, S.C., Roca, R., Weckwerth, T.M., and Andronova, N.G.: Tropospheric water vapor, convection, and climate, Rev. Geophys., 48, RG2001, doi:10.1029/2009RG000301, 2010.

Shi, Y. R., Levy, R. C., Eck, T. F., Fisher, B., Mattoo, S., Remer, L. A., Slutsker, I., and Zhang, J.: Characterizing the 2015 Indonesia fire event using modified MODIS aerosol retrievals, Atmos. Chem. Phys., 19, 259–274, https://doi.org/10.5194/acp-19-259-2019, 2019.

Smirnov, A., Royer, A., O'Neill, N. T., and Tarussov, A.: A study of the link between synoptic air mass type and atmospheric optical parameters, J. Geophys. Res., 99(D10), 20967– 20982, doi:10.1029/94JD01719, 1994.

Sobrino, J.A., Li, Z.-L., and Stoll, M. P.: Impact of the atmospheric transmittance and total water vapor content in the algorithms for estimating satellite sea surface temperatures, *IEEE Transactions on Geoscience and Remote Sensing*, vol. 31, no. 5, pp. 946-952, doi: 10.1109/36.263765, 1993.

Späth, F., Behrendt, A., Muppa, S. K., Metzendorf, S., Riede, A., and Wulfmeyer, V.: 3-D water vapor field in the atmospheric boundary layer observed with scanning differential absorption lidar, Atmos. Meas. Tech., 9, 1701–1720, https://doi.org/10.5194/amt-9-1701-2016, 2016.

Spyrou C.: Direct radiative impacts of desert dust on atmospheric water content, Aerosol Science and Technology, 52:6, 693-701, DOI: 10.1080/02786826.2018.1449940, 2018.

Stull, R. B. and Eloranta, E. W.: Boundary Layer Experiment 1983, Bull. Amer. Meteorol. Soc., 65, 450–456, DOI: 10.1175/1520-0477(1984)065<0450:BLE>2.0.CO;2, 1984.

Su, H., Jiang, J.H., Liu, X., Penner, J.E., Read, W.G., Massie, S., Schoeberl, M.R., Colarco, P., Livesey, N.J., and Santee, M.L.: Observed increase of TTL temperature and water vapor in polluted clouds over Asia, Journal of Climate, 24(11), 2728-2736, https://doi.org/10.1175/2010JCLI3749.1, 2011.

Ten Hoeve, J. E., Remer, L. A., and Jacobson, M. Z.: Microphysical and radiative effects of aerosols on warm clouds during the Amazon biomass burning season as observed by MODIS: impacts of water vapor and land cover, Atmos. Chem. Phys., 11, 3021–3036, https://doi.org/10.5194/acp-11-3021-2011, 2011.

1236 Tesche, M., Gross, S., Ansmann, A., Muller, D., Althausen, D., Freudenthaler, V., and Esselborn, M.: Profiling of
1237 Saharan dust and biomass-burning smoke with multiwavelength polarization Raman lidar at Cape Verde, Tellus B,
1238 63B, 649-676, DOI: 10.1111/j.1600-0889.2011.00548.x, 2011.

1239 Turner D.D., Ferrare, R.A., Heilman Brasseur, L.A., Feltz, W.F., and Tooman, T.P.: Automated Retrievals of Water
1240 Vapor and Aerosol Profiles from an Operational Raman Lidar. J.
1241 Atmos. Oceanic Tech, 19, 37-50, DOI:10.1175/1520-0426(2002), 2002.

1242 Veselovskii, I., Goloub, P., Podvin, T., Bovchaliuk, V., Derimian, Y., Augustin, P., Fourmentin, M., Tanre, D.,
1243 Korenskiy, M., Whiteman, D. N., Diallo, A., Ndiaye, T., Kolgotin, A., and Dubovik, O.: Retrieval of optical and
1244 physical properties of African dust from multiwavelength Raman lidar measurements during the SHADOW
1245 campaign in Senegal, Atmos. Chem. Phys., 16, 7013–7028, doi:10.5194/acp-16-7013-2016, 2016.

1246 Wang, Y., Hua, D., Wang, L., Tang, J., Mao, J., and Kobayashi, T.: Observations and analysis of relationship
1247 between water vapor and aerosols using raman lidar, Jpn. J. Appl. Phys., 51, 102401,
1248 http://dx.doi.org/10.1143/JJAP.51.102401, 2012.

1249 Wang, J., Gei, C., Yang, Z., Hyer, E. J., Reid, J. S., Chew, B. N., Mahmud M.: Mesoscale modeling of smoke
1250 transport over the Southeast Asian Maritime Continent: interplay of sea breeze, trade wind, typhoon, and
1251 topography, Atmos. Res., 122, 486-503, https://doi.org/10.1016/j.atmosres.2012.05.009, 2013.

1252 Wang, H., Xu, J., Zhang, M., Yang, Y., Shen, X., Wang, Y., Chen, D., Guo, J. A Study of the meteorological causes
1253 of a prolonged and severe haze episode in January 2013 over central-eastern China, Atmospheric Environment, 98,
1254 146-157, https://doi.org/10.1016/j.atmosenv.2014.08.053, 2014.

1255 Wang, L. T., Wei, Z., Yang, J., Zhang, Y., Zhang, F. F., Su, J., Meng, C. C., and Zhang, Q.: The 2013 severe haze
1256 over southern Hebei, China: model evaluation, source apportionment, and policy implications, Atmos. Chem. Phys.,
1257 14, 3151–3173, https://doi.org/10.5194/acp-14-3151-2014, 2014.

1258 Wimmers, A. J., C. S. Velden: Seamless Advective Blending of Total Precipitable Water Retrievals from Polar-
1259 Orbiting Satellites. J. Appl. Meteor. Climatol., 50, 1024-1036. doi: http://dx.doi.org/10.1175/2010JAMC2589.1,
1260 2011.

1261 Wong, S., Dessler, A. E., Mahowald, N. M., Yang, P., & Feng, Q.: Maintenance of lower tropospheric temperature
1262 inversion in the Saharan air layer by dust and dry anomaly. Journal of
1263 Climate, 22(19), 5149– 5162. https://doi.org/10.1175/2009jcli2847.1, 2009.

1264 Yu, S., Alapaty, K., Mathur, R. , Pleim, J., Zhang, Y., Nolte, C., Eder, B., Foley, K., and Nagashima, Attribution of
1265 the United States "warming hole": Aerosol indirect effect and precipitable water vapor, Sci Rep, 4, 6929,
1266 https://doi.org/10.1038/srep06929, 2014.

1267 Yu, L., Zhang, M., Wang, L., Lu, Y., and Li, J.: Effects of aerosols and water vapour on spatial-temporal variations
1268 of the clear-sky surface solar radiation in China, Atmospheric Research, 248, 105162,
1269 https://doi.org/10.1016/j.atmosres.2020.105162, 2021.

1270 Yufeng, W., Qiang, F., Meina, Z., Fei, G., Huige, D., Yuehui, S., Dengxin, A.: UV multifunctional Raman lidar
1271 system for the observation and analysis of atmospheric temperature, humidity, aerosols and their conveying
1272 characteristics over Xi'an, J. of Quant Spect. And Rad. Trans, 205, 114-126,
1273 https://doi.org/10.1016/j.jqsrt.2017.10.001, 2018.

1274 Xian, P., Reid, J., Hyer, E., Sampson, C. Rubin, J., Ades, M., Asencio, N., Basart, S., Benedetti, A., Bhattacharjee,
1275 P.S., Brooks, M.E., Colarco, P.R., da Silva, A.M., Eck, T.F., Guth, J., Jorba, O., Kouznetsov, R., Kipling, Z., Sofiev,
1276 M., Perez Garcia-Pando, C., Pradhan, Y., Tanaka, T., Wang, J., Westphal, D.L., Yumimoto, K., and Zhang, J.:
1277 Current state of the global operational aerosol multi-model ensemble: An update from the International Cooperative
1278 for Aerosol Prediction (ICAP). Q.J.R. Meteorol. Soc. 145 (Suppl. 1): 176-209, DOI: 10.1002/qj.3497, 2019.

1279 Xian, P., Klotzbach, P. J., Dunion, J. P., Janiga, M. A., Reid, J. S., Colarco, P. R., and Kipling, Z.: Revisiting the
1280 relationship between Atlantic dust and tropical cyclone activity using aerosol optical depth reanalyses: 2003–2018,
1281 Atmos. Chem. Phys., 20, 15357–15378, https://doi.org/10.5194/acp-20-15357-2020, 2020.

1282 Zeng, Z.-C., Zhang, Q., Natraj, V., Margolis, J. S., Shia, R.-L., Newman, S., Fu, D., Pongetti, T. J., Wong, K. W.,
1283 Sander, S. P., Wennberg, P. O., and Yung, Y. L.: Aerosol scattering effects on water vapor retrievals over the Los
1284 Angeles Basin, Atmos. Chem. Phys., 17, 2495–2508, https://doi.org/10.5194/acp-17-2495-2017, 2017.

1285   Zhang, J., Reid, J.S., Westphal, D.L., Baker, N.L., and Hyer, E.J.: A system for operational aerosol optical depth
1286   data assimilation over global oceans, Journal of Geophysical Research: Atmospheres, 113(D10),
1287   https://doi.org/10.1029/2007JD009065, 2008.

1288   Zhang, J., Wang, S., Guo, Y., Zhang, R., Qin, X., Huang, K., Wang, D., Fu, Q., Wang, J., and Zhou, B.: Aerosol
1289   vertical profile retrieved from ground-based MAX-DOAS observation and characteristic distribution during the
1290   wintertime in Shanghai, China, Atmospheric Environment, 192, 193-205,
1291   https://doi.org/10.1016/j.atmosenv.2018.08.051, 2018.

1292   Zhu, J., Che, H., Xia, X., Yu, X., Wang, J.: Analysis of water vapor effects on aerosol properties and direct radiative
1293   forcing in China, Science of The Total Environment, 650, 257-266, https://doi.org/10.1016/j.scitotenv.2018.09.022,
1294   2019.